Research Square

Preprints are preliminary reports that have not undergone peer review.
They should not be considered conclusive, used to inform clinical practice,
or referenced by the media as validated information.

A topology optimization–based method for the simultaneous design of the structural architectures and actuation patterns of truss walkers with exact frictional contact

Shun Ogawa

ogawa@struct.t.u-tokyo.ac.jp

The University of Tokyo: Tokyo Daigaku https://orcid.org/0009-0006-0480-1309

Katsuyuki Suzuki

The University of Tokyo

Research Article

Keywords: Topology optimization, Ground structure, Frictional contact, Second-order cone complementarity problem, Sensitivity analysis, Automatic differentiation

Posted Date: November 10th, 2026

DOI: https://doi.org/10.21203/rs.3.rs-11670246/v1

License: This work is licensed under a Creative Commons Attribution 4.0 International License.
Read Full License

Additional Declarations: The authors declare no competing interests.

A topology optimization–based method for the simultaneous design of the structural architectures and actuation patterns of truss walkers with exact frictional contact

Shun Ogawa[1*] and Katsuyuki Suzuki[1]

[1*] Department of Systems Innovation, The University of Tokyo, 7-3-1, Hongo, Bunkyo-ku, 113-8656, Tokyo, Japan .

*Corresponding author(s). E-mail(s): ogawa@struct.t.u-tokyo.ac.jp;

Abstract

In this study, a topology optimization–based method is proposed for the simultaneous design of the structural architecture and actuation patterns of a truss walker. In a self-actuated ground locomotion, the structural architecture, which determines the actuator placement, and the actuation patterns, which govern actuator operation, are interdependent; therefore, they must be optimized simultaneously. The design variables comprise the actuator length fraction of each member and the coefficients of truncated Fourier series representing the actuation patterns. These variables are combined into a single design vector, and the travel distance of the mass-weighted center of mass over an evaluation interval is maximized. Because walking is a motion propelled by ground-contact forces, approximating contact conditions during optimization can lead to physically unrealistic designs. To address this issue, frictional contact with the ground is formulated as a single second-order cone complementarity condition that combines the Signorini condition and Coulomb friction. This condition is solved exactly at every time step using a semismooth Newton method and, when it fails to converge, an accelerated primal–dual method. Sensitivity analysis of transient contact problems typically requires the derivation and implementation of adjoint equations. To avoid this, an iteration map is constructed using the consistent Jacobian matrix frozen at the converged solution of each time step. By recording this map once using reverse-mode automatic differentiation and replaying it backward, the exact sensitivity of the implicit function theorem is obtained without deriving or implementing the adjoint equations. Ground contact alone cannot prevent penetration between members. For practical fabrication, each member

must be designated as either an actuator or a structural member. Therefore, a nonpenetration constraint is introduced to prevent member penetration, and a greyness constraint is introduced to enforce binary (0/1) design variables. Both constraints are imposed directly in the optimization problem rather than treated as penalty terms, which guarantees their satisfaction. In the numerical examples, the sensitivities were first validated against finite-difference approximations. Three problems differing only in their initial shape and problems involving an uphill slope and a stepped terrain are solved. In all cases, the proposed method produces walking designs that satisfy the constraints.

Keywords: Topology optimization, Ground structure, Frictional contact, Second-order cone complementarity problem, Sensitivity analysis, Automatic differentiation

1 Introduction

Structures that move via self-actuation have been investigated across various fields, including walking robots, soft robotics, and virtual creatures. Designing such structures requires determining their architecture, i.e., the placement of actuators, and their actuation patterns, i.e., the temporal sequence of actuation. These two aspects are interdependent: the architecture determines the achievable motions, whereas the resulting motion determines the suitability of the architecture. Consequently, methods that optimize one aspect while fixing the other rely on designer experience and trial and error, offering no guarantee of an optimal design under given conditions. Topology optimization [1–3] offers a potential solution to address this issue because it automatically determines optimal structures using governing equations and mathematical optimization. It provides considerable design freedom by optimizing structural geometry and topology such as the number of holes and the presence or absence of structural members. When applied to walking structures, this approach enables the simultaneous optimization of structural architecture and actuation patterns within a unified framework.

Since Sims performed the evolutionary computation of virtual creatures [4], simultaneous structural and motion design has been investigated using gradient-free search centered on evolutionary computation [5, 6]. Recently, hybrid approaches combining evolutionary structural search with deep reinforcement learning for control optimization have also been proposed [6]. However, the computational cost of gradient-free search rapidly increases with increasing number of design variables, limiting the design freedom that can be handled. To address this limitation, differentiable physical simulations that enable gradient-based optimization of physical design parameters such as the material stiffness distributions, together with control variables, have been proposed [7, 8]. Related developments have also been proposed in structural optimization. Sato et al. [9] employed the material point method (MPM) to optimize the structure of a moving soft body, with actuator placement and actuation frequency prescribed. Yuhn et al. [10] proposed 4D topology optimization, which simultaneously

optimizes structural topology and the temporal evolution of self-actuation. These studies demonstrate the feasibility of gradient-based simultaneous design of moving bodies at computational costs suitable for practical applications.

However, these two methods [9, 10] have two limitations. The first concerns the class of structures considered. Both methods target soft bodies represented as continua using the MPM. Although this approach offers substantial design freedom, extending it to large structures remains challenging. This is because soft materials have low stiffness relative to their weight, so that deformation under self-weight increases with size, and because the continuum shapes obtained must be reproduced at that size by molding or additive manufacturing. In contrast, structures composed of structural elements such as trusses can be designed by determining whether each member functions as an actuator. Such designs can also be assembled, regardless of their size, using commercially available structural members and linear actuators. Thus, a simultaneous optimization method for discrete structural systems is required to facilitate scalability. The second limitation concerns contact modeling. Walking relies on contact forces between the structure and the ground; therefore, approximations of the contact conditions can directly affect optimization outcomes. In MPM-based approaches, ground contact is imposed via boundary conditions on the velocities of background-grid nodes [7, 10], rather than by explicitly enforcing the Signorini condition and Coulomb friction as complementarity conditions. More generally, penalty-based contact formulations permit some degree of penetration, and semi-implicit friction treatments that evaluate friction forces using the state of the preceding time step can introduce nonphysical energy transfer due to temporal lag. During optimization, the algorithm may actively exploit errors arising from these approximations, resulting in designs that behave differently from the corresponding physical systems. Therefore, a method is required that simultaneously optimizes structural architecture and actuation patterns for discrete-member structures, enabling easy fabrication and scalability while enforcing the contact conditions exactly at each time step.

Formulating contact conditions as complementarity problems is an established approach in contact mechanics and physical simulation [11, 12]. In particular, Kanno et al. [13] formulated the Signorini condition and Coulomb friction as a second-order cone linear complementarity problem. Subsequently, Kanno [14] introduced a modified gap based on the bipotential of de Saxcé [15], reducing both conditions to a single second-order cone complementarity condition. However, this formulation has not yet been applied to the structural optimization of walking systems.

When contact conditions are enforced exactly in the forward analysis, sensitivity analysis becomes challenging during optimization. The optimization of a walker is a transient problem involving time integration, in which the objective function and constraints depend on the design variables through the entire time history. The discrete adjoint method, based on the discretize-then-differentiate approach, differentiates the time-discretized governing equations directly to obtain sensitivities consistent with the numerical solution. For transient problems, these sensitivities are computed via backward time integration [16]. However, in contact problems, the solution at each time step is governed by complementarity conditions and is therefore only piecewise smooth with respect to the design variables. Sensitivities can be obtained by applying the

implicit function theorem while holding the contact states at the converged solution, including the stick and slip states, fixed [17, 18]. Alternatively, contact forces can be regularized to obtain differentiable formulations [19]; however, such approaches retain the limitations associated with the contact approximations described above. Implementing the discrete adjoint method manually requires deriving and coding the adjoint equations, their right-hand sides, the matrices describing the dependence on the preceding time step, and the chain-rule expressions linking the state variables to the design variables. This derivation must account for member models, contact conditions, and evaluation functions and must be repeated whenever the problem formulation changes.

To address these challenges, a topology optimization–based method for simultaneously designing the structural architecture and actuation patterns of a truss-based walker is proposed herein. Truss structures can be assembled from commercially available structural members and linear actuators, and their dimensions can be scaled by adjusting member lengths. The proposed method has three main features. First, the actuator length fraction of each member and the coefficients of the truncated Fourier series describing the actuation patterns are combined into a single design vector. The structural architecture and actuation patterns are optimized simultaneously using an interior-point method [20]. Second, the Signorini condition and Coulomb friction are formulated as a single second-order cone complementarity condition [14, 15]. This condition is solved exactly at each time step using a semismooth Newton method [21, 22], with an accelerated primal–dual method [14] applied when the former fails to converge. Third, automatic differentiation [23, 24] is employed in forward and sensitivity analyses. In the forward analysis, internal forces and the tangent stiffness matrix are obtained by automatically differentiating the member energy. For sensitivity analysis, an iteration map is constructed using the consistent Jacobian matrix frozen at the converged solution of each time step. This map is recorded only once using reverse-mode automatic differentiation and then replayed backward in time. This approach obtains the exact sensitivity of the implicit function theorem without requiring the manual derivation and implementation of the internal forces, tangent stiffness matrix, or adjoint equations. In addition, nonpenetration constraints that prevent interpenetration between members and a greyness constraint that enforces binary (0/1) designs are imposed as optimization constraints rather than treated as penalty terms or enforced via postoptimization rounding, which guarantees their satisfaction. The proposed sensitivity analysis is validated in numerical examples by comparison with finite-difference estimates. Three problems differing only in their initial configurations and additional problems differing only in terrain are solved. Results demonstrate that the proposed method can generate walking designs that satisfy the imposed constraints.

2 Modeling of the truss walker and governing equations

2.1 Modeling of the members

The walker is modeled as a truss structure comprising nodes arranged on a grid and connected by axial members. This truss arrangement defines the ground structure in which the type of each member is treated as a design variable, as described in Section 4. Let d denote the spatial dimension, n_v the number of nodes, and n_e the number of members. The position of node i is denoted by $\boldsymbol{q}_i \in \mathbb{R}^d$, and $\boldsymbol{q} \in \mathbb{R}^{dn_v}$ denotes the vector collecting the positions of all nodes. The model is a discrete structure comprising only nodal lumped masses and axial members, with no bending or surface elements. The formulation is applicable to arbitrary spatial dimensions. However, all numerical examples described herein are two-dimensional ($d = 2$); their ground-structure configurations are described in Section 7.1.

Each member e is modeled as an axial element with axial rigidity $(EA)_e$ and a time-dependent rest length determined by its target length ratio $\bar{a}_e(t)$. The current length l_e and rest length $l_{r,e}(t)$ of member e are defined as follows.

$$l_e = \|\boldsymbol{q}_{i_1} - \boldsymbol{q}_{i_2}\|\,, \tag{1}$$

$$l_{r,e}(t) = \bar{a}_e(t)\, l_{0,e} \tag{2}$$

Here, $i_1(e)$ and $i_2(e)$ denote the nodes at the two ends of member e and $l_{0,e}$ denotes the initial length of member e, i.e., its length in the initial configuration. A target length ratio of $\bar{a}_e = 1$ indicates that the rest length equals the initial length, whereas $\bar{a}_e < 1$ indicates that the rest length is shorter than the initial length. This change in rest length generates the actuation force that drives the walker. The axial rigidity $(EA)_e$ and target length ratio $\bar{a}_e(t)$ of a member are determined in Section 4.1 from the fractions of structural material and actuator constituting each member.

Mass is lumped at the nodes. The mass of each member is distributed equally between its two end nodes, and the mass of node i is defined as follows.

$$m_i = \frac{1}{2} \sum_{e=1}^{n_e} \chi_{ie}\, \gamma_e\, l_{0,e} \tag{3}$$

Here, γ_e denotes the line density of member e and χ_{ie} is an incidence indicator that equals 1 if node i is an endpoint of member e and 0 otherwise. This lumping scheme exactly preserves the total mass of the members. Moreover, provided that the center of mass of each member is located at its midpoint, it also correctly reproduces the overall center of mass and translational momentum.

2.2 Representation of the actuation pattern

Here, $\hat{a}_e(t)$ denotes the target length ratio of the actuator itself; its relation to the target length ratio $\bar{a}_e(t)$ of the member is defined in Section 4.1. The time-dependent target length ratio $\hat{a}_e(t)$ of actuator e, which defines its actuation pattern, is

represented by a truncated Fourier series composed with a logistic function as follows.

$$z_e(t) = c_{e,0} + \sum_{j=1}^{H} \Big[c^{\mathrm{c}}_{e,j} \cos(2\pi f j t) + c^{\mathrm{s}}_{e,j} \sin(2\pi f j t) \Big], \tag{4}$$

$$\hat{a}_e(t) = a_{\min} + \frac{a_{\max} - a_{\min}}{1 + \exp\big(-z_e(t)\big)} \tag{5}$$

Here, H is the harmonic order, f is the fundamental frequency, and $a_{\min}$ and $a_{\max}$ are the lower and upper bounds of the target length ratio, respectively. The coefficients $\boldsymbol{c} = \{c_{e,0},\ c^{\mathrm{c}}_{e,j},\ c^{\mathrm{s}}_{e,j}\}$ $(j = 1, \ldots, H)$ are referred to as the actuation coefficients, and their number of components is $n_{\mathrm{cf}} = n_e(1 + 2H)$. The truncated Fourier series ensures that the target length ratio is periodic and smooth in time, and the logistic function constrains the target length ratio to the interval $[a_{\min}, a_{\max}]$ for arbitrary coefficient values. Unlike a clamp function, Equation (5) is differentiable and does not introduce gradient discontinuities. The time constant and the force–velocity relation of the actuator during contraction are not considered herein.

2.3 Potential energy

The strain energy of each member is formulated using logarithmic strain to account for finite deformations. The strain energy of member e is defined as follows.

$$E_e(\boldsymbol{q}, t) = \frac{k_e\, \bar{a}_e(t)}{2}\, \varepsilon_e^2, \tag{6}$$

$$\varepsilon_e = \ln \frac{l_e}{l_{r,e}(t)}, \tag{7}$$

$$k_e = (EA)_e\, l_{0,e} \tag{8}$$

Here, ε_e is the logarithmic strain along the member axis, measured relative to its rest length $l_{r,e}(t)$, and k_e is the stiffness coefficient of the member. As $k_e \bar{a}_e = (EA)_e\, l_{r,e}$, Eq. (6) represents the strain energy of a one-dimensional Hencky material, obtained by integrating the strain energy density $\frac{1}{2}(EA)_e \varepsilon_e^2$ over the rest length. This energy satisfies $E_e = 0$ and $\partial E_e / \partial l_e = 0$ when $l_e = l_{r,e}$, and the tangent stiffness at the rest length is $\partial^2 E_e / \partial l_e^2 = (EA)_e / l_{r,e}$. Moreover, because ε_e^2 diverges as $l_e \to 0$, the member length cannot reach zero. The gravitational potential energy is defined as follows.

$$E_{\mathrm{g}}(\boldsymbol{q}) = -\sum_{i=1}^{n_v} m_i\, \boldsymbol{g} \cdot \boldsymbol{q}_i \tag{9}$$

Here, $\boldsymbol{g} \in \mathbb{R}^d$ is the gravitational acceleration vector and m_i is the nodal mass defined by Eq. (3). The total potential energy is the sum of the strain energies (6) of all

members and the gravitational potential (9) as follows.

$$E(\boldsymbol{q}, t) = \sum_{e=1}^{n_e} E_e(\boldsymbol{q}, t) + E_{\mathrm{g}}(\boldsymbol{q}) \tag{10}$$

2.4 Time discretization

Let h be the time step, and let $\boldsymbol{q}^n$ and $\boldsymbol{v}^n$ be the nodal positions and velocities, respectively, at time $t_n = nh$. In the absence of contact, the transition from time t_n to t_{n+1} is formulated as the minimization of an incremental potential as follows [25, 26].

$$\boldsymbol{q}^{n+1} = \arg\min_{\boldsymbol{q}} \Phi_n(\boldsymbol{q}), \tag{11}$$

$$\Phi_n(\boldsymbol{q}) = \frac{1}{2} \sum_{i=1}^{n_v} m_i \left\| \boldsymbol{q}_i - \hat{\boldsymbol{y}}_i \right\|^2 + h^2 E(\boldsymbol{q}, t_{n+1}), \tag{12}$$

$$\hat{\boldsymbol{y}}_i = \boldsymbol{q}_i^n + h\, \boldsymbol{v}_i^n \tag{13}$$

Here, $\Phi_n(\boldsymbol{q})$ is the incremental potential and $\hat{\boldsymbol{y}}_i$ is the predicted position of node i under inertia alone, in the absence of external forces. The stationarity condition $\nabla \Phi_n = \boldsymbol{0}$ can be expressed as follows.

$$m_i \frac{\boldsymbol{q}_i^{n+1} - \boldsymbol{q}_i^n - h\, \boldsymbol{v}_i^n}{h^2} = -\nabla_{\boldsymbol{q}_i} E(\boldsymbol{q}^{n+1}, t_{n+1}) \tag{14}$$

This formulation corresponds to the backward Euler method, in which the internal forces are evaluated at time t_{n+1}. The nodal velocities are then updated as follows.

$$\boldsymbol{v}^{n+1} = \frac{\boldsymbol{q}^{n+1} - \boldsymbol{q}^n}{h} \tag{15}$$

2.5 Frictional contact conditions

The ground is modeled as a plane passing through the origin. The gap between node j and the ground is defined as follows.

$$g_j(\boldsymbol{q}) = \hat{\boldsymbol{n}}^{\mathsf{T}} \boldsymbol{q}_j \tag{16}$$

Here, $\hat{\boldsymbol{n}} \in \mathbb{R}^d$ is the unit normal vector to the ground. Let $\hat{\boldsymbol{t}}_1, \ldots, \hat{\boldsymbol{t}}_{d-1}$ denote an orthonormal basis spanning the tangent plane to the ground. The contact force acting on node j is expressed as follows.

$$\boldsymbol{f}_j = -r_{\mathrm{n},j}\, \hat{\boldsymbol{n}} + \sum_{k=1}^{d-1} r_{\mathrm{t},j,k}\, \hat{\boldsymbol{t}}_k \tag{17}$$

Here, $r_{\mathrm{n},j}$ denotes the normal component of the contact reaction, and $r_{\mathrm{t},j,k}$ denotes the k-th component of its tangential component $\boldsymbol{r}_{\mathrm{t},j} \in \mathbb{R}^{d-1}$. The local contact-force

components are collected into the vector $\boldsymbol{r}_j = (r_{\mathrm{n},j}, \boldsymbol{r}_{\mathrm{t},j})^\mathsf{T} \in \mathbb{R}^d$. The sign convention follows a previous study [14], with compression represented by $r_{\mathrm{n},j} \leq 0$. The friction cone is defined as follows.

$$\mathcal{F}_\mu = \left\{ (r_\mathrm{n}, \boldsymbol{r}_\mathrm{t})^\mathsf{T} \in \mathbb{R}^d : \|\boldsymbol{r}_\mathrm{t}\| \leq -\mu\, r_\mathrm{n} \right\} \tag{18}$$

Here, μ denotes the coefficient of friction. The set $\mathcal{F}_\mu$ is a closed convex cone obtained via a linear transformation of the second-order cone in $\mathbb{R}^d$. For $d = 2$, the tangential component is scalar and the cone reduces to the wedge-shaped region $|r_\mathrm{t}| \leq -\mu r_\mathrm{n}$. The tangential displacement over one time step is defined as follows.

$$\Delta \boldsymbol{u}_{\mathrm{t},j} = \left(\hat{\boldsymbol{t}}_1^\mathsf{T} (\boldsymbol{q}_j^{n+1} - \boldsymbol{q}_j^n),\ \ldots,\ \hat{\boldsymbol{t}}_{d-1}^\mathsf{T} (\boldsymbol{q}_j^{n+1} - \boldsymbol{q}_j^n) \right)^\mathsf{T} \tag{19}$$

The contact conditions comprise the following three requirements. The first is the Signorini condition, which enforces nonpenetration and is expressed as follows.

$$g_j \geq 0, \qquad r_{\mathrm{n},j} \leq 0, \qquad g_j\, r_{\mathrm{n},j} = 0 \tag{20}$$

This condition ensures that a node does not penetrate the ground and that a normal reaction arises only when contact occurs. The second is the friction-cone condition, $\boldsymbol{r}_j \in \mathcal{F}_\mu$, which requires the magnitude of the tangential reaction to be no greater than μ times the magnitude of the normal reaction. The third is the maximum dissipation condition, i.e., the slip rule, which is expressed as follows when $\Delta \boldsymbol{u}_{\mathrm{t},j} \neq \boldsymbol{0}$.

$$\boldsymbol{r}_{\mathrm{t},j} = \mu\, r_{\mathrm{n},j}\, \frac{\Delta \boldsymbol{u}_{\mathrm{t},j}}{\|\Delta \boldsymbol{u}_{\mathrm{t},j}\|} \tag{21}$$

During sliding, the tangential reaction lies on the boundary of the friction cone and acts opposite to the slip direction. Coulomb friction is a nonassociated constitutive law, and the work performed by the sliding friction force depends on the slip path. Consequently, contact and friction cannot be incorporated into the incremental potential in Eq. (12) as energy terms while retaining a single minimization formulation for each time step [11].

The three contact conditions can be combined into a single second-order cone complementarity condition by introducing a modified gap based on the bipotential formulation of de Saxcé [15] [14]. The resulting complementarity condition is given as follows.

$$\mathcal{F}_\mu^* \ni \begin{bmatrix} -\tilde{g}_j \\ \Delta \boldsymbol{u}_{\mathrm{t},j} \end{bmatrix} \perp \begin{bmatrix} r_{\mathrm{n},j} \\ \boldsymbol{r}_{\mathrm{t},j} \end{bmatrix} \in \mathcal{F}_\mu, \tag{22}$$

$$\tilde{g}_j = g_j(\boldsymbol{q}^{n+1}) + \mu\, \|\Delta \boldsymbol{u}_{\mathrm{t},j}\| \tag{23}$$

Here, $\tilde{g}_j$ denotes the modified gap, $\boldsymbol{a} \perp \boldsymbol{b}$ denotes the orthogonality condition $\boldsymbol{a}^\mathsf{T}\boldsymbol{b} = 0$, and $\mathcal{F}_\mu^*$ denotes the dual cone of $\mathcal{F}_\mu$, defined as follows.

$$\mathcal{F}_\mu^* = \left\{ (v_\mathrm{n}, \boldsymbol{v}_\mathrm{t})^\mathsf{T} \in \mathbb{R}^d : v_\mathrm{n} \leq -\mu\, \|\boldsymbol{v}_\mathrm{t}\| \right\} \tag{24}$$

Therefore, the cone inclusion on the left-hand side of Eq. (22) requires $\tilde{g}_j \geq \mu \|\Delta \boldsymbol{u}_{\mathrm{t},j}\|$, which is equivalent to the nonpenetration condition $g_j \geq 0$. When $\Delta \boldsymbol{u}_{\mathrm{t},j} = \boldsymbol{0}$, we have $\tilde{g}_j = g_j$. The normal component of Eq. (22) then reduces to the Signorini condition. Moreover, the orthogonality condition $-\tilde{g}_j r_{\mathrm{n},j} + \Delta \boldsymbol{u}_{\mathrm{t},j}^{\mathsf{T}} \boldsymbol{r}_{\mathrm{t},j} = 0$ imposes no condition on the tangential reaction other than $\boldsymbol{r}_j \in \mathcal{F}_\mu$, so the tangential reaction is arbitrary inside the friction cone, corresponding to the sticking state. When $\mu = 0$, the formulation reduces to frictionless contact.

Accordingly, the governing equations for a time step with contact comprise the stationarity condition of the incremental potential, without explicit contact terms, and Eq. (22).

$$\nabla \Phi_n(\boldsymbol{q}^{n+1}) = \boldsymbol{T} \boldsymbol{\rho}^{n+1}, \tag{25}$$

$$\mathcal{F}_\mu^* \ni \begin{bmatrix} -\tilde{g}_j(\boldsymbol{q}^{n+1}) \\ \Delta \boldsymbol{u}_{\mathrm{t},j} \end{bmatrix} \perp \begin{bmatrix} \rho_{\mathrm{n},j}^{n+1} \\ \boldsymbol{\rho}_{\mathrm{t},j}^{n+1} \end{bmatrix} \in \mathcal{F}_\mu \quad (j = 1, \ldots, n_{\mathrm{ct}}) \tag{26}$$

Here, Φ_n denotes the incremental potential defined in Eq. (12) and $\boldsymbol{\rho}_j = h^2 \boldsymbol{r}_j$ denotes the contact reaction multiplied by the square of the time step. The sparse matrix $\boldsymbol{T}$ transforms the local components of $\boldsymbol{\rho}_j$ into forces in the global coordinate system, incorporating the sign convention in Eq. (17). n_{ct} is the number of candidate contact nodes, and the superscript $n+1$ denotes quantities evaluated at time t_{n+1}. Since the friction cones are invariant under positive scaling, replacing $\boldsymbol{r}_j$ with $\boldsymbol{\rho}_j$ does not alter the complementarity condition in Eq. (22). The velocity update remains identical to that in Eq. (15). Collecting Eq. (26) over all candidate contact nodes yields the following formulation.

$$\mathcal{K}_\mu^* \ni \boldsymbol{\zeta}(\boldsymbol{q}^{n+1}) \perp \boldsymbol{\rho}^{n+1} \in \mathcal{K}_\mu \tag{27}$$

Here, $\boldsymbol{\zeta}(\boldsymbol{q}^{n+1}) \in \mathbb{R}^{d n_{\mathrm{ct}}}$ collects the vectors $(-\tilde{g}_j(\boldsymbol{q}^{n+1}),\ \Delta \boldsymbol{u}_{\mathrm{t},j})^{\mathsf{T}}$ for all candidate contact nodes. $\mathcal{K}_\mu = \mathcal{F}_\mu \times \cdots \times \mathcal{F}_\mu$ denotes the Cartesian product of n_{ct} friction cones, and $\mathcal{K}_\mu^*$ denotes its dual cone.

3 Numerical solution of a time step with frictional contact

The governing equations for a single time step, (25) and (26), derived in Section 2, form a nonlinear system involving complementarity conditions. This section presents a numerical method for solving this system exactly at each time step while enforcing the contact conditions via the complementarity formulation. The method is applicable to arbitrary spatial dimensions d.

3.1 Semismooth Newton method

Because the governing equations, (25) and (26), contain complementarity conditions, they are nonsmooth and cannot be solved directly using the conventional Newton method. Herein, a semismooth Newton method is employed. It applies the equivalence between the primal–dual active-set method and the semismooth Newton method

established by Hintermüller et al. [21] for complementarity problems to contact problems [27]. The complementarity condition in the normal direction can be reformulated as the following equivalent equation [21].

$$g \geq 0, \quad \lambda_{\mathrm{n}} \geq 0, \quad \lambda_{\mathrm{n}} g = 0 \quad \Longleftrightarrow \quad C(\lambda_{\mathrm{n}}, g) := \lambda_{\mathrm{n}} - \max\bigl(0,\ \lambda_{\mathrm{n}} - c\, g\bigr) = 0 \tag{28}$$

Here $\lambda_{\mathrm{n}} = -r_{\mathrm{n}} \geq 0$ denotes the normal reaction multiplier, with compression taken as positive, g is the gap, and $c > 0$ is an arbitrary constant. The equation is written for a single candidate contact node and the node index j is omitted. The function $\max(0, \cdot)$ is nondifferentiable at $\lambda_{\mathrm{n}} - c\, g = 0$, where the contact state changes. The semismooth Newton method addresses this nonsmoothness by replacing the conventional Jacobian matrix with a generalized derivative. At differentiable points, it coincides with the ordinary derivative. For the piecewise linear function $\max(0, t)$, the generalized derivative is 1 for $t > 0$ and 0 for $t \leq 0$. If the generalized derivative at the solution is nonsingular for semismooth equations, the method achieves local superlinear convergence that is similar to the ordinary Newton method [28]. Hintermüller et al. [21] defined the active set of conditions imposed as equalities as follows.

$$\mathcal{A}_k = \left\{\, j : \lambda_{\mathrm{n},j}^k - c\, g_j^k > 0 \,\right\} \tag{29}$$

Here, k denotes the iteration number of the semismooth Newton method, j is the index of a candidate contact node, and $\lambda_{\mathrm{n},j}^k$ and g_j^k are the normal reaction multiplier and gap of node j at iteration k, respectively. Hintermüller et al. [21] showed that the primal–dual active-set method, which imposes $g_j = 0$ for nodes in $\mathcal{A}_k$ and $\lambda_{\mathrm{n},j} = 0$ for nodes outside this set, is equivalent to the semismooth Newton method applied to Eq. (28). Thus, selecting a branch of the generalized derivative corresponds to determining the contact state of each node. Each iteration of the semismooth Newton method determines the contact state of each node from the sign of its trial value and then performs a Newton iteration on the resulting smooth system of equations, with the contact states held fixed.

Following Hüeber et al. [22], the friction condition is formulated as a projection equation that projects the trial tangential traction onto a ball. The trial tangential traction is defined as follows.

$$\hat{\boldsymbol{\lambda}}_{\mathrm{t},j} = \boldsymbol{\lambda}_{\mathrm{t},j} + c\, \Delta \boldsymbol{u}_{\mathrm{t},j}, \tag{30}$$

$$\boldsymbol{\lambda}_{\mathrm{t},j} = -\boldsymbol{r}_{\mathrm{t},j} \tag{31}$$

Here, $\hat{\boldsymbol{\lambda}}_{\mathrm{t},j}$ denotes the trial tangential traction of node j and $\boldsymbol{\lambda}_{\mathrm{t},j}$ denotes the tangential reaction multiplier. The trial normal multiplier used to define the active set (29) is defined as follows.

$$\hat{\lambda}_{\mathrm{n},j} = \lambda_{\mathrm{n},j} - c\, g_j \tag{32}$$

For nodes in the active set, $\hat{\lambda}_{\mathrm{n},j} > 0$. The corresponding projection equation is given as follows.

$$\boldsymbol{\lambda}_{\mathrm{t},j} = \max\Bigl(1,\ \frac{\bigl\|\hat{\boldsymbol{\lambda}}_{\mathrm{t},j}\bigr\|}{\mu \hat{\lambda}_{\mathrm{n},j}}\Bigr)^{-1} \hat{\boldsymbol{\lambda}}_{\mathrm{t},j} \tag{33}$$

The right-hand side represents the projection of $\hat{\boldsymbol{\lambda}}_{\mathrm{t},j}$ onto a ball of radius $\mu\hat{\lambda}_{\mathrm{n},j}$. At convergence, $g_j = 0$ and hence $\hat{\lambda}_{\mathrm{n},j} = \lambda_{\mathrm{n},j}$. If $\left\|\hat{\boldsymbol{\lambda}}_{\mathrm{t},j}\right\| \leq \mu\hat{\lambda}_{\mathrm{n},j}$, then the node is in the sticking state and $\Delta\boldsymbol{u}_{\mathrm{t},j} = \mathbf{0}$ is imposed. Otherwise, the node is in the sliding state and the following condition is imposed.

$$\boldsymbol{\lambda}_{\mathrm{t},j} = \mu\lambda_{\mathrm{n},j}\,\boldsymbol{\sigma}_j, \qquad \boldsymbol{\sigma}_j = \frac{\hat{\boldsymbol{\lambda}}_{\mathrm{t},j}}{\left\|\hat{\boldsymbol{\lambda}}_{\mathrm{t},j}\right\|} \tag{34}$$

Here, $\boldsymbol{\sigma}_j$ is the unit vector representing the slip direction. For $d = 2$, it reduces to the sign ± 1 of $\hat{\lambda}_{\mathrm{t},j}$.

Accordingly, at each semismooth Newton iteration, every candidate contact node is classified as free, sticking, or sliding based on the trial values at the current iterate $(\boldsymbol{q}, \boldsymbol{\rho})$. A Newton iteration is applied to the following system of equations with the contact classifications held fixed.

$$\begin{aligned}
&\nabla\Phi_n(\boldsymbol{q}) - \boldsymbol{T}\boldsymbol{\rho} = \mathbf{0}, \\
&\rho_{\mathrm{n},j} = 0, \quad \boldsymbol{\rho}_{\mathrm{t},j} = \mathbf{0} && (j:\ \text{free}), \\
&g_j(\boldsymbol{q}) = 0, \quad \Delta\boldsymbol{u}_{\mathrm{t},j} = \mathbf{0} && (j:\ \text{stick}), \\
&g_j(\boldsymbol{q}) = 0, \quad \boldsymbol{\rho}_{\mathrm{t},j} - \mu\,\rho_{\mathrm{n},j}\,\boldsymbol{\sigma}_j = \mathbf{0} && (j:\ \text{slip})
\end{aligned} \tag{35}$$

Here, $\boldsymbol{q}$ and $\boldsymbol{\rho}$ are the nodal positions and contact reactions, respectively, at the current iterate and $\boldsymbol{q}^n$ is the nodal position at the previous time step. For $d = 2$, $\boldsymbol{\sigma}_j$ is constant and takes the value ± 1. For $d = 3$, $\boldsymbol{\sigma}_j$ depends on the unknowns; therefore, its derivative must be included when linearizing the equations associated with the sliding state [22]. The linearization of the first equation in Eq. (35) involves the Hessian of the incremental potential, defined as follows.

$$\nabla^2\Phi_n = \boldsymbol{M} + h^2\nabla^2 E \tag{36}$$

Here, $\boldsymbol{M} = \mathrm{diag}(m_i)$ denotes the mass matrix. For a sufficiently small time step, the inertial contribution dominates the Hessian, making it positive definite and nonsingular even when the tangent stiffness $\nabla^2 E$ is singular. The internal force vector ∇E and tangent stiffness matrix $\nabla^2 E$ are computed by differentiating the member energies E_e in Eq. (6), member by member, using forward-mode automatic differentiation [23, 24]. Thus, only the member energy needs to be implemented in the forward analysis. The internal forces and the tangent stiffness matrix are generated automatically, eliminating the need to rederive them when the member model changes. The constant c does not affect the solution set; it changes only the convergence path of the iteration.

3.2 Accelerated primal–dual method

The semismooth Newton method is locally convergent and may fail to converge because of active-set cycling, particularly at candidate contact nodes with nearly zero normal reactions. In such cases, the accelerated primal–dual method proposed by Kanno [14] is

employed. It is an accelerated Chambolle–Pock-type primal–dual method [29], extending the accelerated Uzawa method for frictionless contact problems [30] to problems involving friction. Each iteration comprises three successive operations: a dual update, a primal update, and an acceleration step. First, the dual variables are updated, and the resulting trial reactions are projected onto the friction cone. The trial reactions are calculated as follows.

$$\rho_{\mathrm{n},j}^{\mathrm{tr}} = \rho_{\mathrm{n},j} + \alpha\big(\hat{g}_j + \mu\,\|\Delta\boldsymbol{u}_{\mathrm{t},j}\|\big), \tag{37}$$

$$\boldsymbol{\rho}_{\mathrm{t},j}^{\mathrm{tr}} = \boldsymbol{\rho}_{\mathrm{t},j} - \alpha\,\Delta\hat{\boldsymbol{u}}_{\mathrm{t},j} \tag{38}$$

Here, j denotes the index of a candidate contact node and $\boldsymbol{\rho}_j = (\rho_{\mathrm{n},j}, \boldsymbol{\rho}_{\mathrm{t},j})^{\mathsf{T}}$ denotes the reaction of node j at the current iterate. $\hat{g}_j$ and $\Delta\hat{\boldsymbol{u}}_{\mathrm{t},j}$ are the gap and tangential displacement increment, respectively, at the extrapolated point $\hat{\boldsymbol{q}}$. $\Delta\boldsymbol{u}_{\mathrm{t},j}$ is the tangential displacement increment at the current iterate, and α is the dual step size. The bracketed expression in the normal component includes the gap at the extrapolated point and the friction-dependent term of the modified gap defined by (23). The orthogonal projection of the trial reaction onto the friction cone $\mathcal{F}_\mu$ is obtained in closed form. To express this projection, λ_1 and λ_2 are first defined as follows.

$$\lambda_1 = -\mu\,\rho_{\mathrm{n},j}^{\mathrm{tr}} - \left\|\boldsymbol{\rho}_{\mathrm{t},j}^{\mathrm{tr}}\right\|, \tag{39}$$

$$\lambda_2 = -\rho_{\mathrm{n},j}^{\mathrm{tr}} + \mu\left\|\boldsymbol{\rho}_{\mathrm{t},j}^{\mathrm{tr}}\right\| \tag{40}$$

The projected reaction is determined according to the signs of λ_1 and λ_2 as follows.

$$\boldsymbol{\rho}_j \leftarrow \begin{cases} \boldsymbol{\rho}_j^{\mathrm{tr}} & (\lambda_1 \geq 0), \\ \mathbf{0} & (\lambda_2 \leq 0), \\ \Big(-\dfrac{\lambda_2}{1+\mu^2},\ \dfrac{\mu\lambda_2}{1+\mu^2}\,\dfrac{\boldsymbol{\rho}_{\mathrm{t},j}^{\mathrm{tr}}}{\left\|\boldsymbol{\rho}_{\mathrm{t},j}^{\mathrm{tr}}\right\|}\Big)^{\mathsf{T}} & (\text{otherwise}) \end{cases} \tag{41}$$

In the first case, the trial reaction lies inside the friction cone; thus, the projection is the trial reaction itself. In the second case, it lies inside the polar cone, $-\mathcal{F}_\mu^*$, i.e., the dual cone with its sign reversed, and its projection is the origin. In the third case, the projection lies on the lateral surface of the friction cone. Next, the primal variables are updated using the proximal map as follows.

$$\boldsymbol{q} \leftarrow \mathrm{prox}_{\beta\Phi_n}(\boldsymbol{\omega}) = \arg\min_{\boldsymbol{w}}\Big[\Phi_n(\boldsymbol{w}) + \frac{1}{2\beta}\,\|\boldsymbol{w}-\boldsymbol{\omega}\|^2\Big], \tag{42}$$

$$\boldsymbol{\omega} = \boldsymbol{q} + \beta\,\boldsymbol{T}\boldsymbol{\rho} \tag{43}$$

Here, β is the step size of the primal variables and $\boldsymbol{\omega}$ is the point obtained by adding the displacement induced by the reactions. Finally, the step sizes and extrapolated

point are updated to accelerate convergence as follows.

$$\theta = \frac{1}{\sqrt{1 + \mu_\Phi \beta}}, \tag{44}$$

$$\alpha \leftarrow \alpha / \theta, \tag{45}$$

$$\beta \leftarrow \beta \theta, \tag{46}$$

$$\hat{\boldsymbol{q}} \leftarrow \boldsymbol{q} + \theta \left(\boldsymbol{q} - \boldsymbol{q}_{\mathrm{prev}} \right) \tag{47}$$

Here, θ is the acceleration coefficient, μ_Φ is the strong convexity parameter of Φ_n, and $\boldsymbol{q}_{\mathrm{prev}}$ is the primal variable of the previous iteration.

Unlike the primal problem discussed in Ref. [14], which is formulated as a quasistatic quadratic optimization problem, the present method uses the incremental potential Φ_n defined in Eq. (12) as its primal objective. The following expression is used for its strong convexity parameter.

$$\mu_\Phi = \frac{1}{2} \min_i m_i \tag{48}$$

Here, i is the node index and m_i is the nodal mass. The minimization problem in Eq. (42) is solved using a modified Newton method. If the Hessian is not positive definite, a positive diagonal regularization term is added to obtain a positive-definite approximation. A line-search process is also employed. Let Ψ be the objective function of the minimization problem on the right-hand side of Eq. (42). Convergence is assessed using the following relative gradient criterion, normalized by the gradient norm at the initial point.

$$\max_i \left\| \nabla_{\boldsymbol{q}_i} \Psi(\boldsymbol{w}) \right\| \leq \varepsilon_{\mathrm{r}} \max_i \left\| \nabla_{\boldsymbol{q}_i} \Psi(\boldsymbol{w}^{(0)}) \right\| \tag{49}$$

Here, $\nabla_{\boldsymbol{q}_i} \Psi$ is the gradient of Ψ with respect to the position of node i, $\boldsymbol{w}^{(0)}$ is the initial point of the modified Newton method, and ε_{r} is the relative tolerance. Even if the modified Newton method reaches its iteration limit without satisfying this criterion, the primal variables are updated using the solution obtained at that iteration. Convergence of the overall time step is assessed using the residual criteria defined in Section 3.3. The reactions from the preceding time step are used as the initial values of the dual variables.

3.3 Convergence criteria and procedure for a single time step

Figure 1 shows the computational procedure for a single time step with contact. After determining the target length ratios at time t_{n+1} from the actuation coefficients, the semismooth Newton method is first applied with a maximum of n_{P} iterations, where n_{P} is the iteration limit of the semismooth Newton method. Let $\boldsymbol{F}(\boldsymbol{q}, \boldsymbol{\rho})$ denote the residual given by the left-hand side of Eq. (35). The current iterate is accepted as the solution of the time step if it satisfies the following criterion and all the contact-residual tolerances defined below.

$$\left\| \boldsymbol{F}(\boldsymbol{q}, \boldsymbol{\rho}) \right\|_\infty < \max\left(\varepsilon_{\mathrm{F},0},\ \varepsilon_{\mathrm{F},1}\, h^2 \max_e k_e \right) \tag{50}$$

Here, $\varepsilon_{\mathrm{F},0}$ denotes the absolute tolerance, $\varepsilon_{\mathrm{F},1}$ the relative tolerance with respect to the member stiffness, and k_e the stiffness coefficient of member e, defined in Eq. (8). The force-balance components of the residual correspond to the gradient of the incremental potential. Their numerical errors scale with h^2 and the member stiffness coefficients. Thus, the residual tolerance is scaled by the stiffness, as defined in Eq. (50).

If the semismooth Newton method fails to converge, the accelerated primal–dual method is iterated until convergence. Its convergence is judged by the change in the primal variables between successive iterations as follows.

$$\|\boldsymbol{q} - \boldsymbol{q}_{\mathrm{prev}}\|_\infty < \varepsilon_q + \varepsilon_{q,\mathrm{r}}\, \|\boldsymbol{q} - \boldsymbol{q}^n\|_\infty \tag{51}$$

Here, ε_q and $\varepsilon_{q,\mathrm{r}}$ are the absolute and relative tolerances, respectively, and $\boldsymbol{q}^n$ is the nodal position at the previous time step. The iteration is also terminated when the iteration limit n_{PD} is reached, in which case the solution at that iteration is used. The initial step sizes are $\alpha = \alpha_0$ and $\beta = 1/\alpha_0$. The semismooth Newton method is then restarted from the primal–dual solution to further reduce the residual to machine precision. In either case, the following three contact residuals are evaluated.

$$r_{\mathrm{pen}} = \max_j \max(0,\ -g_j), \tag{52}$$

$$r_{\mathrm{fric}} = \max_j \frac{\|\boldsymbol{r}_{\mathrm{t},j}\| + \mu\, r_{\mathrm{n},j}}{-\mu\, r_{\mathrm{n},j}}, \tag{53}$$

$$r_{\mathrm{comp}} = \max_j \left|(-\tilde{g}_j,\ \Delta\boldsymbol{u}_{\mathrm{t},j})\,(r_{\mathrm{n},j},\ \boldsymbol{r}_{\mathrm{t},j})^{\mathsf{T}}\right| \tag{54}$$

Here, r_{pen} is the penetration residual, r_{fric} is the relative friction-cone violation, r_{comp} is the complementarity residual, and j is the index of a candidate contact node. The maximum in the definition of r_{fric} is taken over contact nodes with $r_{\mathrm{n},j} < 0$. g_j, $\tilde{g}_j$, $\Delta\boldsymbol{u}_{\mathrm{t},j}$, $r_{\mathrm{n},j}$, and $\boldsymbol{r}_{\mathrm{t},j}$ denote the gap, modified gap, tangential displacement increment, normal reaction, and tangential reaction of node j, respectively, as defined in Section 2.5. If any of these residuals exceed its tolerance, the analysis is regarded as failed and the optimization is aborted. The residuals of the governing equations at each time step are reduced to machine precision because the sensitivity analysis described in Section 5 relies on the implicit function theorem, which requires the governing equations to be satisfied at the converged solution.

4 Design problem

4.1 Definition of the design variables

The design problem simultaneously determines actuator placement and actuation patterns to maximize the distance traveled within a prescribed time. Each member is classified as either a structural member that supports the body or an actuator member that generates driving force by shortening its rest length in response to a command. An actuator is an element that replaces part or all of a member and extends or contracts axially, such as a linear actuator or a pneumatic artificial muscle. The actuator placement is represented by the design variable x_e, which denotes the fraction of the

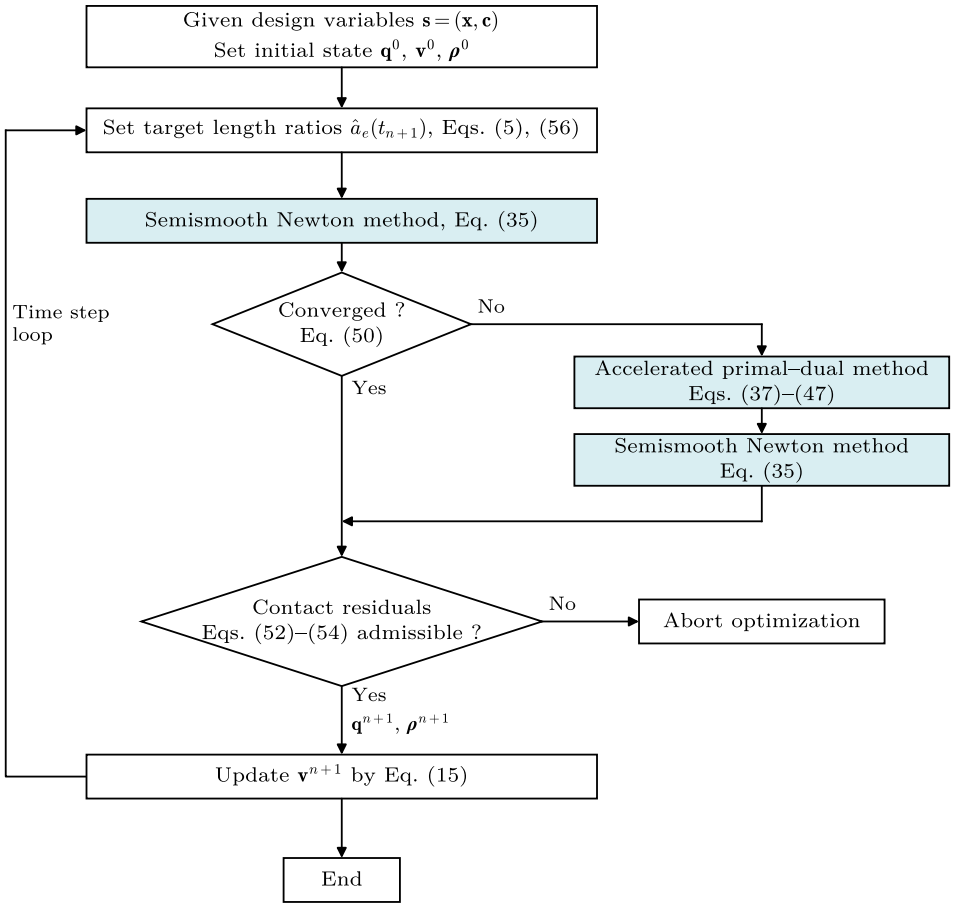


Fig. 1: Computational procedure for the contact analysis at a single time step. Cyan boxes denote the procedures employed to solve the governing equations with frictional contact conditions.

initial length of member e occupied by the actuator. Thus, $x_e = 1$ represents a member composed entirely of an actuator over its full length, $x_e = 0$ represents a member comprising only structural material, and x_e takes continuous values in $0 \leq x_e \leq 1$. The axial rigidity, target length ratio, and line density of a member with an intermediate value of x_e are obtained by interpolating the properties of the two end points as follows.

$$\frac{1}{(EA)_e} = \frac{1-x_e}{E^{\mathrm{s}}A} + \frac{x_e}{E^{\mathrm{m}}A}, \tag{55}$$

$$\bar{a}_e(t) = (1-x_e) + x_e\,\hat{a}_e(t), \tag{56}$$

$$\gamma_e = (1-x_e)\,\gamma^{\mathrm{s}} + x_e\,\gamma^{\mathrm{m}} \tag{57}$$

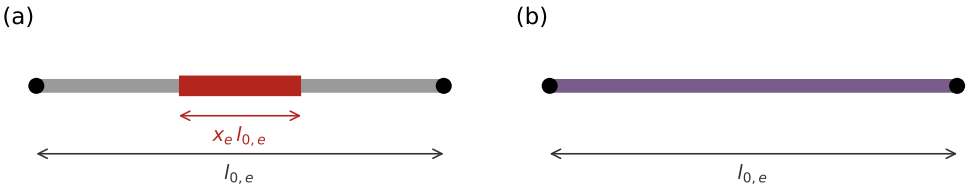


Fig. 2: Interpretation of the design variable x_e. (a) Member e comprising a structural segment of length $(1 - x_e)\, l_{0,e}$ (grey) and an actuator segment of length $x_e\, l_{0,e}$ (red) connected in series. (b) The corresponding single axial element used in the model.

Here, $E^{\mathrm{s}}A$ and $E^{\mathrm{m}}A$ denote the axial rigidities of the structural member and actuator, respectively; E^{s} and E^{m} are their Young's moduli, respectively; and A is the cross-sectional area. $\hat{a}_e(t)$ is the actuator target length ratio defined in Section 2.2. $\gamma^{\mathrm{s}} = \rho^{\mathrm{s}}A$ and $\gamma^{\mathrm{m}} = \rho^{\mathrm{m}}A$ are the line densities of the structural member and actuator, respectively. ρ^{s} and ρ^{m} are their respective mass densities. Equation (55) gives the harmonic mean of the axial rigidities, and Eqs. (56) and (57) use linear interpolation. As shown in Fig. 2, these interpolations reproduce the small-strain stiffness at the initial configuration as well as the rest length and mass for arbitrary $\hat{a}_e$ of a member comprising a structural segment of length $(1 - x_e)\, l_{0,e}$ and an actuator segment of length $x_e\, l_{0,e}$ connected in series along the member axis. Thus, an intermediate value of x_e represents a member in which part of the structural segment is replaced by an actuator. When the actuator contracts to the target length ratio $\hat{a}_e$, the rest length of the member decreases by $x_e(1 - \hat{a}_e)\, l_{0,e}$. If the actuator is positioned at the center of the member, the center of mass of the member remains at its midpoint, and the equal mass distribution described in Section 2.1 holds. As Eq. (55) yields the axial rigidity of the series connection, an interpolation that penalizes intermediate properties such as in the solid isotropic material with penalization (SIMP) method [1] is not used. Note that the nodal masses in Eq. (3) depend on x_e; therefore, the self-weight is a design-dependent load [31]. From a fabrication viewpoint, each member is ultimately required to be either a structural member or an actuator. Accordingly, x_e is driven toward 0 or 1 by imposing an upper bound on the greyness measure defined in Section 4.5. Once the greyness constraint is satisfied and the design variables are binary, the motion analysis of the final design is independent of the interpolation method.

The weights of the Fourier series defining the actuator motion in Eq. (4) are also treated as design variables. The interval $[c_{\min}, c_{\max}]$ for the actuation coefficients is chosen sufficiently wide to allow the logistic function in Eq. (5) to reach saturation.

Therefore, the design variables considered herein are defined as follows.

$$\boldsymbol{s} = (\boldsymbol{x}, \boldsymbol{c}) \in [0,1]^{n_e} \times [c_{\min}, c_{\max}]^{n_{\mathrm{cf}}} \tag{58}$$

Here, $\boldsymbol{x} = (x_1, \ldots, x_{n_e})$ and n_{cf} is the number of components of $\boldsymbol{c}$. Combining the structural design variables $\boldsymbol{x}$ and the actuation-pattern design variables $\boldsymbol{c}$ into a single design vector enables the structural architecture and actuation patterns to be

simultaneously updated within the same optimization problem. Thus, the optimization problem simultaneously determines the actuator placement and the motion of each actuator.

4.2 Travel distance

The travel distance is defined as the displacement of the mass-weighted center of mass X_{c} over the evaluation interval, defined as follows.

$$D(\boldsymbol{s}) = X_{\mathrm{c}}(t_N) - X_{\mathrm{c}}(t_0), \tag{59}$$

$$X_{\mathrm{c}}(t_k) = \frac{\sum_{i=1}^{n_v} m_i \, q_{i,x}^k}{\sum_{i=1}^{n_v} m_i} \tag{60}$$

Here, N denotes the number of time steps in the evaluation interval and $q_{i,x}^k$ is the x coordinate of node i at time t_k. Because the nodal masses m_i depend on the design variables based on Eq. (3), the objective D depends explicitly on the design variables based on the mass distribution in addition to its implicit dependence through the trajectory. The travel distance is maximized by maximizing the objective function in Eq. (59).

4.3 Maximum penetration

The contact conditions described in Section 2.5 are imposed only between the nodes and ground; contact between members is not considered. Therefore, when a member shortens and a node approaches and passes through another member, no contact resistance is generated. The optimization may therefore exploit such physically unrealistic configurations. The grid-shaped truss is subdivided into simplices: triangles for $d = 2$ and tetrahedra for $d = 3$. Thus, penetration can be regarded as a vertex of a simplex crossing the face opposite to that vertex, corresponding to an inversion of the simplex. To quantify this possibility, a clearance measure based on the distance from each simplex vertex to its opposite face is defined. The case $d = 2$ is described below.

Let the vertices of triangle t be (i_1, i_2, i_3), ordered so that the signed area is positive in the initial configuration. The signed area at time t_k is defined as follows.

$$A_t(\boldsymbol{q}^k) = \frac{1}{2}\left[(\boldsymbol{q}_{i_2}^k - \boldsymbol{q}_{i_1}^k) \times (\boldsymbol{q}_{i_3}^k - \boldsymbol{q}_{i_1}^k)\right] \tag{61}$$

Here, $\boldsymbol{a}\times\boldsymbol{b} = a_x b_y - a_y b_x$. Let $l_{t,v}(\boldsymbol{q}^k)$ denote the current length of the member opposite vertex i_v $(v = 1, 2, 3)$. The signed distance from vertex i_v to the line containing the opposite member is given as follows.

$$\delta_{k,t,v} = \frac{2A_t(\boldsymbol{q}^k)}{l_{t,v}(\boldsymbol{q}^k)} \tag{62}$$

$\delta_{k,t,v}$ represents the clearance between the vertex and line containing the opposite member. For $d = 3$, the clearance is defined as $\delta_{k,t,v} = 3V_t/A_{t,v}$, where V_t is the signed volume of tetrahedron t and $A_{t,v}$ is the area of the face opposite vertex i_v. In the following, each simplex t is assumed to have $d + 1$ vertices, regardless of the spatial dimension. $\delta_{k,t,v} = 0$ indicates that the vertex lies in the plane containing the opposite face, and $\delta_{k,t,v} < 0$ indicates that the vertex has crossed that plane, corresponding to an inverted simplex. Let $\delta_{\min}$ be the lower bound of the clearance. The nonpenetration requirement is imposed at every time step t_k in the evaluation interval, for every simplex t, and for each of its vertices v, as follows.

$$\delta_{k,t,v} \geq \delta_{\min} \qquad (k = 1, \ldots, N;\ t = 1, \ldots, n_t;\ v = 1, \ldots, d + 1) \tag{63}$$

n_t is the number of simplices. The condition $\delta_{\min} > 0$ excludes configurations in which a vertex lies on the plane containing its opposite face. Because clearance has dimensions of length, the lower bound $\delta_{\min}$ can be set as a design requirement according to the required member thickness and joint dimensions. To ensure that the initial configuration satisfies Eq. (63), $\delta_{\min} < \delta_{0,t,v}$ is taken with respect to the clearance $\delta_{0,t,v} = \delta_{k,t,v}\big|_{k=0}$ of the initial configuration.

Equation (63) comprises $(d + 1)\, n_t N$ inequality constraints. Imposing these constraints individually in the optimization problem would considerably increase the computational cost of the sensitivity analysis (Section 5). This is because reverse-mode automatic differentiation would require a separate reverse replay for each constraint. To evaluate the satisfaction of Eq. (63) using a single scalar quantity, the constraints are aggregated using an L^p norm approach [32]; this approach has also been used to aggregate stress constraints. Unlike the method proposed by Le et al., however, no adaptive normalization factor is employed. Instead, the lower bound is incorporated into the normalization as follows. First, the clearance margin relative to the lower bound is normalized so that it is 0 in the initial configuration and equal to 1 at the lower bound. The normalized margin is defined as follows.

$$s_{k,t,v} = \frac{\delta_{0,t,v} - \delta_{k,t,v}}{\delta_{0,t,v} - \delta_{\min}} \tag{64}$$

Because $\delta_{\min} < \delta_{0,t,v}$, the denominator is positive. Consequently, $s_{k,t,v} \leq 1$ and $\delta_{k,t,v} \geq \delta_{\min}$ are equivalent. Thus, Eq. (63) can be rewritten as $\max_{k,t,v} s_{k,t,v} \leq 1$. The maximum is approximated using a differentiable L^p norm. However, $s_{k,t,v}$ is negative when the clearance at a vertex increases relative to its initial value. Raising these values to the power p_A would not preserve their sign; therefore, the following smooth positive-part function is introduced. p_A is an even integer.

$$s^+_{k,t,v} = \frac{1}{2}\left(s_{k,t,v} + \sqrt{s^2_{k,t,v} + \varepsilon_A^2}\right) \tag{65}$$

Here, ε_A is a small positive number, and $s^+_{k,t,v} > 0$ and $s^+_{k,t,v} \geq s_{k,t,v}$ hold. The L^p norm of $s^+_{k,t,v}$ aggregated over all times, simplices, and vertices is then defined as the

maximum-penetration measure as follows.

$$\Pi(\boldsymbol{s}) = \left(\sum_{k=1}^{N} \sum_{t=1}^{n_t} \sum_{v=1}^{d+1} \left(s_{k,t,v}^{+}\right)^{p_A} \right)^{1/p_A} \tag{66}$$

p_A is the aggregation exponent. The resulting quantity Π provides a smooth upper bound on $\max_{k,t,v} s_{k,t,v}$. Based on the mathematical properties of the L^p norm, the following inequality holds.

$$\max_{k,t,v} s_{k,t,v} \leq \max_{k,t,v} s_{k,t,v}^{+} \leq \Pi(\boldsymbol{s}) \tag{67}$$

Therefore, if $\Pi \leq 1$, then Eq. (63) is satisfied for all k, t, and v. Accordingly, $\Pi \leq 1$ is imposed as the nonpenetration constraint in Section 4.6. This constraint is intended to prevent local penetration associated with simplex inversion. However, it does not prevent global self-contact in which large deformations cause spatially distant parts of the body to overlap.

4.4 Actuator volume

The total actuator volume is defined as follows.

$$V(\boldsymbol{x}) = \sum_{e=1}^{n_e} x_e \, l_{0,e} \tag{68}$$

Hereafter, V denotes the total actuator volume. It represents the amount of actuator material used and depends only on the structural design variables. In Section 4.6, an upper bound is imposed on the ratio of V to the total member length $\sum_e l_{0,e}$, thereby defining the actuator-volume constraint.

4.5 Greyness measure

From the viewpoint of manufacturability, each member must be classified as either an actuator or a structural member. Therefore, a greyness measure [10] is introduced to drive the actuator-placement design variables $\boldsymbol{x}$ toward binary values (0 and 1).

$$M(\boldsymbol{x}) = \frac{\sum_{e=1}^{n_e} 4\, x_e(1 - x_e)\, l_{0,e}}{\sum_{e=1}^{n_e} l_{0,e}} \tag{69}$$

The measure M is defined such that M equals 0 when all members have $x_e \in \{0, 1\}$, whereas M equals 1 when all members have $x_e = 0.5$. In Section 4.6, an upper bound on M is imposed to enforce the greyness constraint.

4.6 Optimization problem

The objective is to maximize the travel distance of the walker over an evaluation interval comprising N time steps. The optimization problem considered herein is formulated as follows.

$$\begin{aligned} \underset{\boldsymbol{x},\ \boldsymbol{c}}{\text{maximize}} \quad & D(\boldsymbol{s}) \\ \text{subject to} \quad & \begin{cases} \nabla\Phi_n(\boldsymbol{q}^{n+1}) = \boldsymbol{T}\boldsymbol{\rho}^{n+1}, \\ \mathcal{K}_\mu^* \ni \boldsymbol{\zeta}(\boldsymbol{q}^{n+1}) \perp \boldsymbol{\rho}^{n+1} \in \mathcal{K}_\mu, \\ g_1(\boldsymbol{x}) = \dfrac{V(\boldsymbol{x})}{V_{\max}\sum_e l_{0,e}} - 1 \le 0, \\ g_2(\boldsymbol{s}) = \Pi(\boldsymbol{s}) - 1 \le 0, \\ g_3(\boldsymbol{x}) = M(\boldsymbol{x}) - M_{\max} \le 0, \\ 0 \le x_e \le 1, \\ c_{\min} \le c_\kappa \le c_{\max} \quad (\kappa = 1, \dots, n_{\mathrm{cf}}). \end{cases} \end{aligned} \tag{70}$$

Here, D is the travel distance defined in Eq. (59). The first and second constraints are the governing equations (Eqs. (25) and (27)) that must be satisfied at each time step $n = 0, \dots, N-1$. The constraint $g_1 \le 0$ limits the actuator volume V (Eq. (68)) to at most a fraction $V_{\max}$ of the total member length $\sum_e l_{0,e}$. The constraint $g_2 \le 0$ enforces nonpenetration by limiting the aggregated measure Π (Eq. (66)) to at most 1. This ensures that the clearance remains at least the lower bound $\delta_{\min}$ at all time steps, simplices, and vertices of the evaluation interval (Eq. (63)). The constraint $g_3 \le 0$ limits the greyness measure M (Eq. (69)) to the prescribed upper bound $M_{\max}$. The final two constraints define the ranges of the design variables: $\boldsymbol{x}$, which determines actuator placement, and $\boldsymbol{c}$, which determines actuator patterns.

The upper bound $M_{\max}$ in the greyness constraint $g_3 \le 0$ is not imposed at its final value from the beginning of the optimization. Instead, it is tightened in stages. When all members are assigned the same intermediate initial value, the greyness measure M defined in Eq. (69) is large and the final greyness constraint cannot be satisfied. Therefore, during the first n_{w} iterations, while a forward-moving actuation pattern is being established, the upper bound is set to $M_{\mathrm{s}} = 1$, the maximum value of M. Subsequently, the upper bound is reduced every n_{d} iterations until it reaches the final value $M_{\max}$ at iteration n_{f}. The upper bound in the greyness constraint after ℓ reductions is expressed as follows.

$$M_{\max}^{(\ell)} = M_{\mathrm{s}} \left(\frac{M_{\max}}{M_{\mathrm{s}}} \right)^{t_\ell}, \tag{71}$$

$$t_\ell = \min\left(1,\ \frac{\ell\, n_{\mathrm{d}}}{n_{\mathrm{f}} - n_{\mathrm{w}}}\right). \tag{72}$$

Here, ℓ is the number of reductions applied after the first n_{w} iterations and increases by 1 every n_{d} iterations. In this approach, the greyness constraint drives the binarization of the actuator-placement variables and the staged reduction of its upper bound determines the progression from actuation-pattern formation to design binarization.

After the upper bound reaches its final value, it is held fixed, and the resulting optimization problem retains the constraint $g_3 \leq 0$ with this final upper bound. The optimization problem in Eq. (70) is solved using the interior-point optimization solver, IPOPT [20]. Whenever the upper bound of the greyness constraint is reduced by one stage, IPOPT is restarted using the Lagrange multipliers obtained at the end of the preceding stage as the initial multiplier estimates.

5 Sensitivity analysis

In the gradient-based topology optimization, the sensitivities of the objective function and constraints with respect to the design variables are required to identify an optimal structure. The objective function D and the nonpenetration constraint g_2 depend on the trajectory $\boldsymbol{q}^1, \ldots, \boldsymbol{q}^N$, which is obtained by the time integration of the governing equations (25) and (27). These quantities are collectively referred to as the evaluation function J, whose derivative $\mathrm{d}J/\mathrm{d}\boldsymbol{s}$ with respect to the design vector $\boldsymbol{s}$ is sought. In contrast, volume constraint g_1 and greyness constraint g_3 depend only on the design variables. Therefore, their sensitivities are computed by applying reverse-mode automatic differentiation [23] to the evaluations of Eqs. (68) and (69).

The discrete adjoint method, which differentiates the time-discretized governing equations, provides sensitivities consistent with the numerical discretization. For transient problems, the adjoint equations are solved via backward substitution in time [16]. In the present problem, however, the state at each time step is obtained by solving nonlinear equations containing the contact complementarity conditions. This solution depends implicitly on the design variables and the state at the preceding time step. Applying the discrete adjoint method directly would require analytically deriving and implementing the Jacobian matrix of the residual at each time step, its partial derivatives with respect to the previous state, and the chain rule relating the design variables to the physical quantities. It would also require implementing the backward-in-time solution of the resulting adjoint equations. To avoid these explicit derivations and implementations, the present study adopts the reverse-mode automatic differentiation for fixed-point iterations [33]. For each time step, an iteration map is constructed using the consistent Jacobian matrix frozen at the converged solution. Then, the map is recorded using reverse-mode automatic differentiation, and its derivatives are computed via a reverse replay. In the method proposed by Christianson [33], additional iterations are generally required to obtain the adjoint solution. However, when the frozen matrix is chosen to be the consistent Jacobian matrix at the converged solution, the derivative of the iteration map with respect to the state vanishes at that solution. As also discussed by Christianson [33], a single recording of one evaluation of the iteration map of each time step, rather than of the complete forward trajectory, and a single reverse replay are sufficient. Thus, this approach provides the same sensitivities as the discrete adjoint method without the need to derive or implement the adjoint equations and their right-hand sides.

5.1 Sensitivity of one step

The unknown variables for a time step from t_n to t_{n+1} are collected into the following vector.

$$\boldsymbol{\varphi}^{n+1} = \left(\boldsymbol{q}^{n+1}, \boldsymbol{\rho}^{n+1}\right) \tag{73}$$

The physical quantities determined by the design vector, namely the member stiffness coefficients defined in Eqs. (55) and (8), the nodal masses defined in Eq. (3), and the effective target length ratios of the members at time t_{n+1} defined in Eqs. (56) and (5), are also collected into a vector as follows.

$$\boldsymbol{\theta}^n = \boldsymbol{\theta}^n(\boldsymbol{s}) \tag{74}$$

The governing equations for a single time step are expressed in terms of the following residual.

$$\boldsymbol{R}^n\left(\boldsymbol{\varphi}^{n+1};\ \boldsymbol{w}^n\right) = \boldsymbol{0} \tag{75}$$

$\boldsymbol{w}^n$ is the input of step n, defined as follows.

$$\boldsymbol{w}^n = \left(\boldsymbol{q}^n, \boldsymbol{v}^n, \boldsymbol{s}\right) \tag{76}$$

Here, $\boldsymbol{R}^n$ is the left-hand side of Eq. (35) described in Section 3.1, with the contact states at the converged solution classified as free, sticking, and sliding and then held fixed. The residual depends on the design vector $\boldsymbol{s}$ through the physical quantities defined in Eq. (74). The Jacobian matrix of $\boldsymbol{R}^n$ with respect to $\boldsymbol{\varphi}^{n+1}$ is defined as follows.

$$\boldsymbol{H}^n = \frac{\partial \boldsymbol{R}^n}{\partial \boldsymbol{\varphi}^{n+1}} \tag{77}$$

The matrix $\boldsymbol{H}^n$ is nonsymmetric. Its force-balance rows contain the mass and tangent-stiffness contributions, $\boldsymbol{M} + h^2\boldsymbol{K}_t$, and the reaction terms, whereas its contact rows represent the conditions corresponding to the contact state of each node. Here, $\boldsymbol{K}_t$ denotes the tangent stiffness matrix. In a neighborhood of a solution at which the residual is exactly zero, the implicit function theorem gives the following sensitivity relation.

$$\boldsymbol{H}^n \frac{\mathrm{d}\boldsymbol{\varphi}^{n+1}}{\mathrm{d}\boldsymbol{w}^n} = -\frac{\partial \boldsymbol{R}^n}{\partial \boldsymbol{w}^n} \tag{78}$$

The implicit function theorem is applied locally about a point satisfying $\boldsymbol{R}^n = \boldsymbol{0}$; therefore, before differentiating, the residual at each converged time step is reduced to machine precision, as described in Section 3.3.

In the discrete adjoint implementation based directly on Eq. (78), the right-hand side $\partial \boldsymbol{R}^n / \partial \boldsymbol{w}^n$ must be explicitly derived. This requires calculating the partial derivatives with respect to the state at the preceding time step and applying the chain rule to account for the dependence of the physical quantities on the design variables. In this study, the following iteration map is constructed instead. Let $\boldsymbol{\varphi}_*^{n+1}$ denote the converged solution at time step n obtained via the forward motion analysis. The Jacobian matrix evaluated at this solution is

$$\hat{\boldsymbol{H}}^n = \boldsymbol{H}^n\left(\boldsymbol{\varphi}_*^{n+1}\right) \tag{79}$$

With $\hat{\boldsymbol{H}}^n$ frozen as a constant, the iteration map is defined as follows.

$$\boldsymbol{S}^n(\boldsymbol{\varphi};\ \boldsymbol{w}^n) = \boldsymbol{\varphi} - (\hat{\boldsymbol{H}}^n)^{-1}\,\boldsymbol{R}^n\big(\boldsymbol{\varphi};\ \boldsymbol{w}^n\big) \tag{80}$$

Because $\hat{\boldsymbol{H}}^n$ is nonsingular, the conditions $\boldsymbol{S}^n(\boldsymbol{\varphi};\boldsymbol{w}^n) = \boldsymbol{\varphi}$ and $\boldsymbol{R}^n = \boldsymbol{0}$ are equivalent. Thus, the converged solution is a fixed point of $\boldsymbol{S}^n$.

The iteration map has the property that its derivative with respect to $\boldsymbol{\varphi}$ vanishes at the converged solution. Differentiating Eq. (80) with respect to $\boldsymbol{\varphi}$ yields the following relation.

$$\frac{\partial \boldsymbol{S}^n}{\partial \boldsymbol{\varphi}} = \boldsymbol{I} - (\hat{\boldsymbol{H}}^n)^{-1}\boldsymbol{H}^n \tag{81}$$

As $\boldsymbol{H}^n = \hat{\boldsymbol{H}}^n$ at $\boldsymbol{\varphi} = \boldsymbol{\varphi}_*^{n+1}$, the following holds.

$$\left.\frac{\partial \boldsymbol{S}^n}{\partial \boldsymbol{\varphi}}\right|_{\boldsymbol{\varphi}_*^{n+1}} = \boldsymbol{0} \tag{82}$$

Consequently, the sensitivity of the converged solution with respect to the input can be obtained from a single evaluation of $\boldsymbol{S}^n$. As a function of the input $\boldsymbol{w}^n$, the converged solution satisfies the following identity.

$$\boldsymbol{\varphi}^{n+1}(\boldsymbol{w}^n) = \boldsymbol{S}^n\big(\boldsymbol{\varphi}^{n+1}(\boldsymbol{w}^n);\ \boldsymbol{w}^n\big) \tag{83}$$

Differentiating this identity with respect to $\boldsymbol{w}^n$ yields the following relation.

$$\frac{\mathrm{d}\boldsymbol{\varphi}^{n+1}}{\mathrm{d}\boldsymbol{w}^n} = \frac{\partial \boldsymbol{S}^n}{\partial \boldsymbol{\varphi}}\,\frac{\mathrm{d}\boldsymbol{\varphi}^{n+1}}{\mathrm{d}\boldsymbol{w}^n} + \frac{\partial \boldsymbol{S}^n}{\partial \boldsymbol{w}^n} \tag{84}$$

At the converged solution, the first term on the right-hand side vanishes according to Eq. (82); therefore, the following expression holds.

$$\frac{\mathrm{d}\boldsymbol{\varphi}^{n+1}}{\mathrm{d}\boldsymbol{w}^n} = \left.\frac{\partial \boldsymbol{S}^n}{\partial \boldsymbol{w}^n}\right|_{\boldsymbol{\varphi}_*^{n+1}} \tag{85}$$

In other words, the derivative with respect to the input $\boldsymbol{w}^n$ of a single evaluation of $\boldsymbol{S}^n$ with the converged solution treated as a constant coincides with the sensitivity of the converged solution itself. From Eq. (80), the following expression is obtained.

$$\frac{\partial \boldsymbol{S}^n}{\partial \boldsymbol{w}^n} = -(\hat{\boldsymbol{H}}^n)^{-1}\,\frac{\partial \boldsymbol{R}^n}{\partial \boldsymbol{w}^n} \tag{86}$$

Therefore, Eq. (85) coincides with Eq. (78), obtained from the implicit function theorem.

Note that if the frozen matrix is not the consistent Jacobian at the converged solution, Eq. (82) does not hold. In that case, $\boldsymbol{S}^n$ must be applied repeatedly to obtain Eq. (85) [33]. Herein, the consistent Jacobian matrix at the converged solution is frozen, allowing the sensitivity to be obtained via a single application of the iteration

map. Eq. (85) depends only on the converged solution and not on the iterative path taken by the solvers described in Section 3 to obtain that solution. Because Eq. (35), with the contact states held fixed, defines a locally smooth square system, the preceding argument applies directly. The sticking condition at a contact node depends on the previous state $\boldsymbol{q}^n$; this dependence is also included in the recorded evaluation of the residual. The solution map is piecewise smooth, and its derivative is discontinuous at contact-state transition points. Near such a transition point, the computed sensitivity takes the value of the branch to which the converged solution belongs.

5.2 Sensitivity of the whole time integration

The complete time integration is obtained by composing the following one-step solution map with the velocity update (15) over the time steps $n = 0, \ldots, N-1$.

$$\boldsymbol{q}^{n+1} = \boldsymbol{S}_{\boldsymbol{q}}^n\left(\boldsymbol{\varphi}_*^{n+1};\ \boldsymbol{w}^n\right) \tag{87}$$

Here, $\boldsymbol{S}_{\boldsymbol{q}}^n$ denotes the position component of the map $\boldsymbol{S}^n$. According to Eq. (85), by recording a single evaluation of $\boldsymbol{S}^n$ with the converged solution held fixed using reverse-mode automatic differentiation, its reverse replay computes the transposed action of the sensitivity of the step solution with respect to its input. The gradient of the evaluation function J with respect to the final state is used to initialize the reverse propagation. By successively recording and reverse replaying each step in reverse chronological order from $n = N-1$ to 0, the gradient $\bar{\boldsymbol{s}}$ is propagated back to the design vector. The resulting sensitivity is given as follows.

$$\frac{\mathrm{d}J}{\mathrm{d}\boldsymbol{s}} = \frac{\partial J}{\partial \boldsymbol{s}} + \bar{\boldsymbol{s}} \tag{88}$$

Here, $\partial J/\partial \boldsymbol{s}$ represents the direct dependence of the evaluation function on the design variables, which arises from the mass weighting in Eq. (60).

During the recording, the action of $(\hat{\boldsymbol{H}}^n)^{-1}$ is implemented as the solution of a linear system. In the reverse pass, the corresponding transposed linear system is solved. Let $\bar{\boldsymbol{\varphi}}^{n+1}$ denote the gradient propagated to the converged step solution $\boldsymbol{\varphi}^{n+1}$. The reverse replay of Eq. (80) then corresponds to the following operations.

$$\boldsymbol{\xi}^{n+1} = -(\hat{\boldsymbol{H}}^n)^{-\mathsf{T}}\,\bar{\boldsymbol{\varphi}}^{n+1}, \tag{89}$$

$$\bar{\boldsymbol{w}}^n \leftarrow \bar{\boldsymbol{w}}^n + \left(\frac{\partial \boldsymbol{R}^n}{\partial \boldsymbol{w}^n}\right)^{\mathsf{T}} \boldsymbol{\xi}^{n+1} \tag{90}$$

Here, $\bar{\boldsymbol{w}}^n$ is the gradient propagated to the input $\boldsymbol{w}^n$ of the step. $\boldsymbol{\xi}^{n+1}$ corresponds to the adjoint variable in the discrete adjoint method. Thus, Eqs. (89) and (90) perform the same operations as the backward recurrence of the discrete adjoint method in time. However, the adjoint equations, their right-hand sides, the matrices describing the dependence on the preceding time step, and the chain rule connecting the physical quantities to the design variables are neither derived nor implemented explicitly. Instead, the implementation requires only the residual in Eq. (75), which defines the

equations solved at each time step, and the mapping in Eq. (74), which relates the design vector to the physical quantities.

When the evaluation function also depends on the intermediate states, as g_2 does through all $\boldsymbol{q}^k$ in Eq. (66), the partial derivatives $\partial J/\partial \boldsymbol{q}^n$ and $\partial J/\partial \boldsymbol{v}^n$ are added to $\bar{\boldsymbol{q}}^n$ and $\bar{\boldsymbol{v}}^n$ after the reverse replay of step n before they are passed to the preceding step. The objective function D and the nonpenetration constraint g_2 share the same recorded computational operations. Using a vector-mode reverse replay, in which the output-side gradients are supplied as a vector, their sensitivities are obtained simultaneously from a single recording and reverse replay. Because the recording is created and discarded at each time step, the memory required to store the automatic differentiation tape does not increase with the number of time steps. The automatic differentiation library CoDiPack [24] is used herein.

6 Verification of the sensitivity analysis

6.1 Analysis model and conditions

In gradient-based topology optimization, the quality of optimization results depends on the accuracy of the calculated sensitivities. Therefore, the sensitivity analysis described in Section 5 is verified by comparing its results with numerical derivatives computed over the entire time integration. The sensitivities obtained using central finite differences are computed as follows.

$$\frac{\mathrm{d}J}{\mathrm{d}s_e} \approx \frac{J(\boldsymbol{s} + \Delta s\, \boldsymbol{e}_e) - J(\boldsymbol{s} - \Delta s\, \boldsymbol{e}_e)}{2\Delta s} \tag{91}$$

Here, J is the evaluation function, s_e is the e-th component of the design vector $\boldsymbol{s}$, $\boldsymbol{e}_e$ is the unit vector whose only nonzero component is component e, and Δs is the finite-difference step size. The relative error between the two sensitivity estimates is defined as $|J'_{\mathrm{AD}} - J'_{\mathrm{FD}}| \,/\, |J'_{\mathrm{FD}}|$, where J'_{AD} and J'_{FD} are the sensitivities obtained using automatic differentiation and central finite differences, respectively. Central finite differences require two complete time integrations for each design variable. Thus, their computational cost increases linearly with the number of design variables, making them impractical for large-scale optimization. However, because this approach can be used to estimate sensitivities independently of the evaluation function, it serves as a reference for verifying the sensitivity accuracy.

Figure 3 shows the analysis model used for verification; the members whose sensitivities are reported in Table 1 are numbered in the figure. The model is a grid-shaped truss of 0.45-m width and 0.30-m height. It comprises 3×2 cells measuring 0.15 m $\times$ 0.15 m, identical to that used in the numerical examples described in Section 7, and contains 12 nodes and 23 members. The diagonal members alternate in orientation between adjacent cells. The walker starts its motion from rest, with the nodes in the bottom row initially in contact with the ground. The member model, material properties, time-step size, friction coefficient, harmonic order, fundamental actuation frequency, and target-length-ratio range are identical to those used in the numerical examples shown in Table 2. The lower bound on the clearance in the nonpenetration

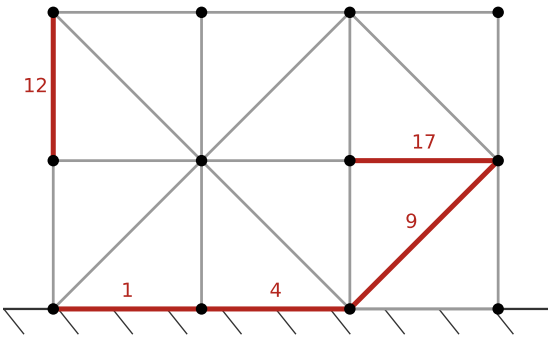


Fig. 3: Analysis model used to verify the sensitivities. The model is a grid-shaped truss comprising 3×2 cells. The numbers indicate the member indices for which the sensitivities are reported in Table 1.

constraint is also set to the same value as in those examples, $\delta_{\min} = 0.02$ m. The evaluation interval comprises $N = 12$ time steps and includes frictional contact. The two evaluation functions considered are the travel distance D and the nonpenetration constraint g_2. Intermediate values are assigned to the design variables to avoid biasing the contact-state distribution or the member properties. The actuator length fractions are prescribed for each member as $x_e = 0.2 + 0.6\,\big|\sin\big(1.7(e-1)\big)\big|$. The actuation coefficients are set to $c_{e,0} = 0$, $c^{\mathrm{c}}_{e,1} = 2\cos\big(2\pi(e-1)/n_e\big)$, $c^{\mathrm{s}}_{e,1} = 2\sin\big(2\pi(e-1)/n_e\big)$, and the coefficients of the second harmonic are set to 0. Here, e is the member index. The total number of design variables is 138. Under these conditions, the contact states of the nodes near the ground over all time steps comprise 23 free, 7 sticking, and 18 sliding states, covering all three contact states. The finite-difference step size is set to $\Delta s = 1.0 \times 10^{-5}$.

6.2 Verification results

Table 1 shows the verification results. The design variables listed in the table include x_e, i.e., the actuator length fraction in member e, and $c_{e,0}$, $c^{\mathrm{c}}_{e,j}$, and $c^{\mathrm{s}}_{e,j}$, i.e., the actuation coefficients of member e in Eq. (4). The positions of the corresponding members are shown in Fig. 3. For the travel distance D and the nonpenetration constraint g_2, the sensitivities with respect to the actuator length fractions x_e and the actuation coefficients $\boldsymbol{c}$ agree with those obtained using central finite differences, with relative errors not exceeding 1.0×10^{-5}. The largest relative error occurs for $c^{\mathrm{s}}_{12,2}$. However, the corresponding sensitivity has a small magnitude, approximately 1.0×10^{-6}, making the relative error more susceptible to numerical rounding error in the finite-difference calculation. These results confirm that the reverse-mode automatic differentiation of the proposed iteration map reproduces the sensitivities obtained from the implicit function theorem even for a problem involving all three contact states.

Table 1: Verification of the sensitivities. Comparison of sensitivities obtained using reverse-mode automatic differentiation (AD) of the iteration map and central finite differences for the travel distance D and the nonpenetration constraint g_2.

Function	Variable	AD	Central difference	Relative error
D	x_1	1.938×10^{-3}	1.938×10^{-3}	2.9×10^{-9}
	x_9	-3.145×10^{-3}	-3.145×10^{-3}	3.2×10^{-9}
	x_{17}	1.931×10^{-3}	1.931×10^{-3}	7.4×10^{-11}
	$c_{1,0}$	7.403×10^{-5}	7.403×10^{-5}	1.9×10^{-7}
	$c^{\mathrm{c}}_{4,1}$	-2.027×10^{-4}	-2.027×10^{-4}	8.1×10^{-8}
	$c^{\mathrm{s}}_{12,2}$	2.036×10^{-6}	2.036×10^{-6}	3.6×10^{-6}
g_2	x_1	-7.227×10^{-3}	-7.227×10^{-3}	1.2×10^{-9}
	x_9	-1.313×10^{-2}	-1.313×10^{-2}	2.6×10^{-11}
	x_{17}	1.562×10^{-2}	1.562×10^{-2}	8.1×10^{-10}
	$c_{1,0}$	9.558×10^{-4}	9.558×10^{-4}	3.9×10^{-10}
	$c^{\mathrm{c}}_{4,1}$	2.836×10^{-3}	2.836×10^{-3}	1.9×10^{-9}
	$c^{\mathrm{s}}_{12,2}$	4.183×10^{-4}	4.183×10^{-4}	1.0×10^{-8}

7 Numerical examples

7.1 Analysis models and conditions

The proposed method is applied to three walking problems: locomotion on flat ground, an uphill slope, and terrain with a step. The three initial configurations, shown in Fig. 4, are square, wide, and tall. All configurations are grid-shaped trusses, as described in Section 2.1, and comprise $n_x \times n_y$ square cells. Each cell has four edge members and one diagonal member. The diagonal-member orientation alternates between adjacent cells. The total number of nodes is $(n_x + 1)(n_y + 1)$. All cells have dimensions of 0.15 m $\times$ 0.15 m. Thus, the three configurations differ only in their numbers of cells and overall dimensions. The gravitational acceleration vector is $\boldsymbol{g} = (0, -g)^{\mathsf{T}}$. For flat-ground locomotion, the ground is represented by the plane $y = 0$, whose normal vector is $\hat{\boldsymbol{n}} = (0, 1)^{\mathsf{T}}$ and tangential vector is $\hat{\boldsymbol{t}}_1 = (1, 0)^{\mathsf{T}}$. The representations of the uphill slope and stepped terrain are described in Sections 7.3 and 7.4, respectively. Table 2 summarizes the material properties and analysis-model parameters, and Table 3 lists the conditions of the numerical analysis and optimization. These conditions are common to all cases; only the initial configuration and terrain differ.

The walker starts from rest, with the nodes in the bottom row initially in contact with the ground. The initial design variables are set to $x_e = 0.5$ for the actuator length fraction of every member, whereas all actuation coefficients are initialized to 0. When all actuation coefficients are 0, the target length ratio is constant and equal to $(a_{\min} + a_{\max})/2$ for every actuator. Thus, the initial design has no prescribed time-varying actuation pattern to generate forward motion; the actuation pattern is formed entirely via optimization.

The axial rigidity of the actuator is $E^{\mathrm{m}}A = 4.2 \times 10^4$ N, which is 0.42 times that of the structural member. The lower bound on the target length ratio is $a_{\min} = 0.85$.

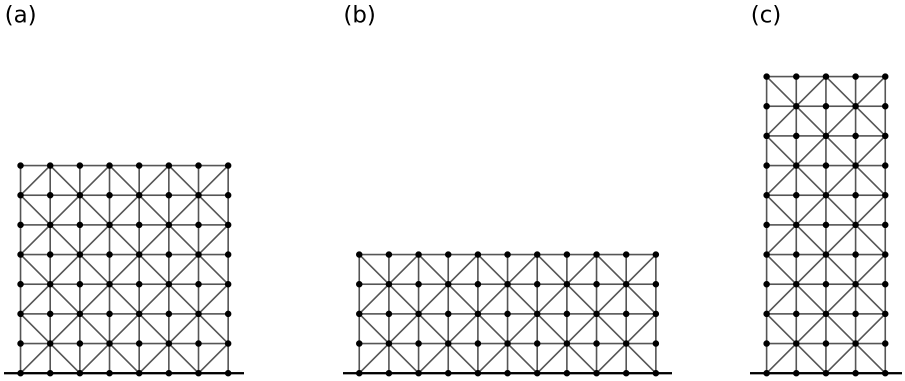


Fig. 4: Initial configurations (ground structures) used in the numerical examples. The cell dimensions are 0.15 m × 0.15 m in all cases. (a) Square (1.05 m × 1.05 m, 7×7 cells, 64 nodes, and 161 members), (b) wide (1.5 m × 0.6 m, 10×4 cells, 55 nodes, and 134 members), (c) tall (0.6 m × 1.5 m, 4×10 cells, 55 nodes, and 134 members).

Table 2: Material properties and analysis-model properties common to all cases.

Item	Symbol	Value	Unit
Axial rigidity of structural member	$E^{\mathrm{s}}A$	1.0×10^5	N
Axial rigidity of actuator	$E^{\mathrm{m}}A$	4.2×10^4	N
Line density of structural member	γ^{s}	5.0	kg/m
Line density of actuator	γ^{m}	7.0	kg/m
Gravitational acceleration	g	9.8	$\mathrm{m/s^2}$
Friction coefficient	μ	0.3	–
Lower and upper bounds of target length ratio	$a_{\min}$, $a_{\max}$	0.85, 1.0	–
Harmonic order of actuation pattern	H	2	–
Fundamental frequency of actuation pattern	f	2.0	Hz
Time-step size	h	0.03	s
Number of time steps in the evaluation interval	N	100	–

Table 3: Numerical-analysis and optimization parameters common to all cases.

Item	Symbol	Value
Relative tolerance of the modified Newton method	ε_{r}	1.0×10^{-4}
Maximum semismooth Newton iterations and constant	n_{P}, c	40, 1
Primal–dual tolerances and iteration limit	ε_q, $\varepsilon_{q,\mathrm{r}}$, n_{PD}	10^{-10}, 10^{-6}, 40000
Initial dual step size	α_0	10
Initial value of actuator-placement variables	x_e	0.5
Lower and upper bounds of actuation coefficients	$c_{\min}$, $c_{\max}$	−8, 8
Upper bound on volume	$V_{\max}$	0.30
Nonpenetration-constraint parameters	$\delta_{\min}$, p_A, ε_A	0.02 m, 16, 10^{-4}
Initial and final upper bounds on the greyness measure	M_{s}, $M_{\max}$	1.0, 0.005
Greyness-bound reduction schedule	n_{w}, n_{d}, n_{f}	80, 16, 420
Maximum number of IPOPT iterations		600

According to Eqs. (55) and (56), an actuator occupying the entire length of a member can shorten its rest length by at most 15% of its initial length. The evaluation interval comprises $N = 100$ time steps, i.e., 3.0 s. This duration covers six periods of the actuation pattern, whose fundamental period is 0.5 s. The lower bound on the clearance in the nonpenetration constraint is $\delta_{\min} = 0.02$ m. In the initial configuration, the minimum clearance $\delta_{0,t,v}$ occurs between a cell vertex and the opposite diagonal member and is given by $0.15/\sqrt{2} \approx 0.106$ m. Thus, the prescribed lower bound is approximately 19% of the initial minimum clearance.

7.2 Effects of the initial model shape

The flat-ground walking problem is solved for all three initial configurations to investigate whether the proposed method can obtain feasible walking designs from different initial shapes. Table 4 shows the optimization results, Fig. 5 shows the optimized designs, and Fig. 6 presents the corresponding motion trajectories over the evaluation interval. As shown in Fig. 6, no member crossings are observed at any time step during the evaluation interval. Furthermore, all three walkers move forward via body flexion and extension without falling over during the simulated interval. As shown in Table 4, the actuator-volume fraction is below its upper bound for all three configurations. The minimum clearance also exceeds the lower bound, and the greyness measure does not exceed its upper bound. Thus, all three designs satisfy the imposed constraints, with the actuator-placement variables being nearly binary.

Figure 5 shows that for all configurations, actuators are located mainly in the bottom-row members in contact with the ground and in the diagonal members connected to them. Most of the upper structure comprises passive structural members. This arrangement concentrates actuation in the regions that generate propulsion by pushing against the ground, whereas the upper structure maintains the walker's posture mainly as a passive frame. The travel distances reported in Table 4 are comparable across the three configurations, with each walker traveling several times its characteristic body dimension. The optimized designs also exhibit a common structural arrangement despite differences in their initial configurations. These results indicate that the proposed method functions regardless of the initial shape.

Figure 7 shows the iteration histories of the objective function and constraints for the tall configuration as a representative example. Because this configuration is narrow relative to its height, its triangular elements are susceptible to inversion during body flexion and extension. Consequently, the effect of the nonpenetration constraint is particularly evident in this case. As shown in Fig. 7(a), a forward-moving actuation pattern emerges early in the optimization, causing the travel distance to increase rapidly. The travel distance is subsequently maintained, although it fluctuates as the design becomes increasingly binary. Figure 7(d) shows that the greyness measure decreases as the upper bound is progressively tightened, eventually reaching the upper bound at the final stage. This behavior indicates that the staged reduction of the upper bound described in Section 4.6 determines the order of actuation-pattern formation and design binarization, as intended. As shown in Fig. 7(c), the nonpenetration constraint g_2 occasionally becomes positive during the optimization iterations. However, it returns to the feasible region in the subsequent iteration, indicating that

Table 4: Optimization results for locomotion on flat ground.

Item	Square	Wide	Tall
Travel distance D (m)	5.58	5.95	5.08
Actuator-volume fraction $V/\sum_e l_{0,e}$ (upper bound 0.30)	0.263	0.287	0.236
Minimum clearance δ_{true} (m, lower bound 0.02)	0.038	0.075	0.043
Greyness measure M (upper bound 0.005)	0.0050	0.0049	0.0050

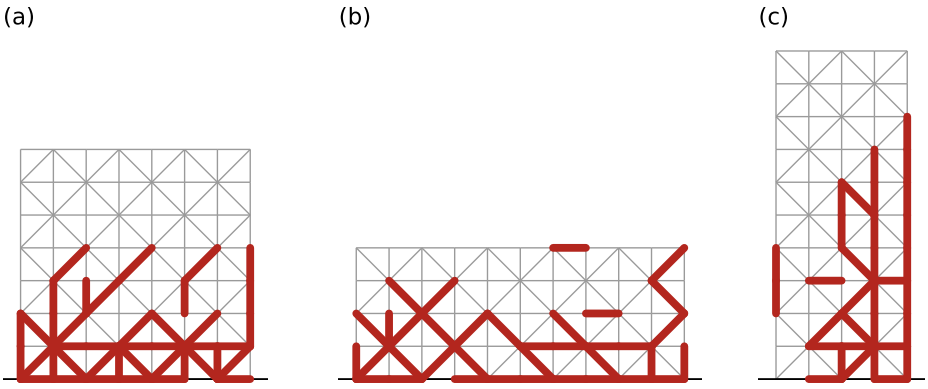


Fig. 5: Final designs. (a) Square, (b) wide, and (c) tall. Grey denotes structural members and red denotes actuator members.

the corresponding simplex inversions are resolved each time. The grey bands in Fig. 7 indicate iteration intervals in which IPOPT could not identify an acceptable step size during the line search and entered its feasibility-restoration phase to reduce constraint violations [20]. During this phase, IPOPT solves an auxiliary problem rather than performing a regular optimization iteration. Consequently, the objective and constraint functions in these intervals are not directly comparable with those from regular iterations; therefore, they are excluded from the plots.

7.3 Study on a slope

The walker's ability to climb a uniform slope is investigated by modifying only the terrain in the square-design problem. The slope is represented by rotating the gravity vector while keeping the ground horizontal, as follows.

$$\boldsymbol{g} = g\,(-\sin\theta,\ -\cos\theta)^{\mathsf{T}} \tag{92}$$

This is equivalent to rotating the coordinate system to align it with the slope. Herein, a slope with an inclination of $\theta = 10^\circ$ is considered. The contact conditions described in Section 2.5 retain the same form as those for flat ground, and the travel distance D (Eq. (59)) is measured along the slope. The only change to the governing equations is the direction of $\boldsymbol{g}$ in the gravitational potential (9); the sensitivity analysis remains

Table 5: Optimization results for locomotion on an uphill slope.

Item	Slope
Travel distance D (m)	2.41
Volume fraction $V/\sum_e l_{0,e}$ (upper bound: 0.30)	0.295
Minimum clearance δ_{true} (m, lower bound: 0.02)	0.064
Greyness measure M (upper bound: 0.005)	0.0050

the same as that described in Section 5. Except for the terrain, all other conditions are identical to those listed in Tables 2 and 3.

Figure 8 shows the final design and its motion over the evaluation interval. The optimization produces a structure that climbs the slope without difficulty, raising its center of mass against gravity. As shown in Fig. 8(b), the walker moves forward along the slope and its center of mass rises in the vertical direction. No member crossings occur during the evaluation interval. As shown in Table 5, the volume, nonpenetration, and greyness constraints are all satisfied, and the optimized member design variables are binary (0/1). As shown in Fig. 8(a), the actuators are concentrated mainly on the ground-facing side of the structure, as in the flat-ground case.

7.4 Study on a step

The walker's ability to move forward over a step in the direction of travel is investigated herein. The ground profile is described by the following height function.

$$h(x) = \frac{r}{2}\left[1 + \tanh\frac{x - x_{\text{s}}}{w_{\text{s}}}\right] \tag{93}$$

Here, r is the step height, x_{s} is the horizontal position of the step, and w_{s} is the width of the corner rounding. The corners are rounded to ensure that the ground normal is uniquely defined at the step edges, so that the contact conditions and their derivatives are defined. The gap between node j and the ground as well as the normal and tangent of the local contact coordinate system are defined as follows.

$$g_j = q_{j,y} - h(q_{j,x}), \tag{94}$$

$$\hat{\boldsymbol{n}} = \frac{(-h',\ 1)^{\mathsf{T}}}{\sqrt{1+h'^2}}, \qquad \hat{\boldsymbol{t}}_1 = \frac{(1,\ h')^{\mathsf{T}}}{\sqrt{1+h'^2}} \tag{95}$$

Here, h' is the derivative of the ground-height function. The local contact coordinate system is evaluated at the nodal position $\boldsymbol{q}^n$ at the beginning of each time step and is then held fixed during that step. The gap is evaluated at the current nodal position. The remaining contact conditions are identical to those described in Section 2.5. Because the local contact coordinate system depends on the preceding state $\boldsymbol{q}^n$, this dependence is included when propagating sensitivities to the preceding time step. In

Table 6: Optimization results for locomotion over a step.

Item	Step
Travel distance D (m)	2.74
Volume fraction $V/\sum_e l_{0,e}$ (upper bound 0.30)	0.236
Minimum clearance δ_{true} (m, lower bound 0.02)	0.031
Greyness measure M (upper bound 0.005)	0.0050

the present formulation, this contribution is captured automatically by differentiating the residual evaluation described in Section 5.1. Thus, automatic differentiation accounts for this dependence in the sensitivity calculation.

Figure 9 shows the ground profile. The step height is $r = 0.04$ m, approximately one-quarter of the cell size. The corner-rounding width is $w_{\mathrm{s}} = 0.05$ m, and the step is located at $x_{\mathrm{s}} = 2.05$ m, 1.0 m ahead of the front end of the walker. The maximum slope of the rounded step face is $\arctan\bigl(r/(2w_{\mathrm{s}})\bigr) \approx 21.8^\circ$, which exceeds the friction angle 16.7° for the friction coefficient $\mu = 0.3$. All conditions other than the terrain are identical to those listed in Tables 2 and 3.

Figure 10 shows the optimized design and its motion over the evaluation interval. As shown in Fig. 10(b), all nodes of the walker pass over the step during the latter half of the evaluation interval, after which the walker continues moving forward on top of the step. As the maximum slope of the rounded step face exceeds the friction angle, static friction alone cannot support a node on the face under gravity. Therefore, the walker appears to pass over the step face by the inertia of its motion. As shown in Table 6, the volume, nonpenetration, and greyness constraints are all satisfied. No member crossings occur during the evaluation interval. The optimized member design variables are also close to binary values (0/1). These results indicate that the proposed method can produce a walker that traverses stepped terrain while accounting for the contact conditions.

8 Conclusion

Herein, a topology optimization–based design method was proposed that simultaneously determines the structural architecture and actuation pattern of a truss walker to maximize its travel distance over a given time interval. The main contributions of this study are as follows. First, focusing on truss structures, which are easy to fabricate and scale up, the actuator fraction of each member and the Fourier coefficients defining the actuation patterns were treated as a single design-variable vector. The structural architecture and actuation patterns were simultaneously optimized using a gradient-based method.

Second, frictional contact with the ground was formulated without penalty or smoothing approximation and enforced exactly at every time step as a second-order cone complementarity problem. The exact treatment of frictional contact introduces nonsmoothness via transitions among contact, sticking, and sliding states. Deriving and implementing the corresponding adjoint equations has conventionally been a major barrier to sensitivity analysis.

Third, automatic differentiation was applied to both the forward and sensitivity analyses. In the forward analysis, internal forces and tangent stiffness matrices were obtained via the automatic differentiation of the member energy. In the sensitivity analysis, the reverse-mode automatic differentiation of an iteration map constructed with the consistent Jacobian matrix frozen at the converged solution was employed. This approach enabled computing sensitivities equivalent to those obtained using the discrete adjoint method, without manually deriving the adjoint equations. The implementation requires the member energy, residual equations for each time step, mapping from design variables to physical quantities, and objective and constraint evaluation functions. Consequently, the gradient calculations do not need to be rederived manually when the member model or contact conditions are modified.

By combining the exact treatment of frictional contact, exact sensitivity analysis, and the simultaneous optimization of structural architecture and actuation patterns, binary (0/1) walker designs that satisfied the constraints and avoided member crossings were obtained. These results were demonstrated on flat ground, an inclined surface, and stepped terrain without changing the optimization framework. The main findings and remaining challenges are summarized below.

- A walker model was developed in which each member is represented as a series connection of a structural member and an actuator and formulated as a finite-deformation axial element using logarithmic strain. Frictional contact with the ground was formulated as a second-order cone complementarity problem based on the bipotential of de Saxcé. The resulting motion-analysis problem was solved exactly at every time step using a combination of the semismooth Newton method and the accelerated primal–dual method.
- A design-optimization problem was formulated to maximize travel distance subject to volume, greyness, and nonpenetration constraints. The nonpenetration constraint was defined via a lower bound on the clearance between each simplex vertex and its opposite face and evaluated using an L^p-norm aggregation with the constraint bound incorporated into the formulation. By reducing the upper bound on the greyness measure in stages, the design was binarized without hindering the formation of the actuation patterns. The constraints were imposed as constraints rather than enforced via penalty terms or postoptimization rounding, which guaranteed their satisfaction.
- Three design problems under identical conditions but with different initial configurations were solved. In all three cases, designs with nearly binary (0/1) member variables were obtained. The resulting walkers moved while satisfying all the constraints and avoiding member crossings.
- The method was also applied to uphill-slope and step-terrain problems. In both cases, walkers capable of traversing the terrain were obtained, even for terrains unfavorable for locomotion. This shows that the proposed method yields effective structures according to the terrain.
- The proposed optimization problem is nonconvex; therefore, the obtained solutions are local optima. Algorithms to identify better optima for such problems must be developed. The present model also neglects actuator contraction dynamics and material damping. Furthermore, member-intersection prevention is limited to local

penetration control by the lower bound of the clearance within a simplex; global self-contact between distant parts of the walker is not considered. Future work will focus on addressing these limitations.

Supplementary information

Videos (MP4 format) showing the motion over the evaluation interval in Figs. 6, 8, and 10 are provided in the supplementary material. The file names correspond to the numbers of the respective figures.

Declarations

Funding

This work was supported by JSPS KAKENHI Grant Number JP26K17293.

Author contributions

Shun Ogawa contributed to the conception and design of the study, developed the method, implemented the code, and performed the numerical computations. Shun Ogawa prepared the first draft of the manuscript, and Katsuyuki Suzuki reviewed and commented on previous versions of the manuscript. All authors read and approved the final manuscript.

Conflict of interest

On behalf of all authors, the corresponding author declares that they have no conflicts of interest.

Ethics approval and consent to participate

Not applicable.

Data availability

Data will be made available on request.

Replication of results

The information necessary to reproduce the results is provided in the manuscript. Further details regarding the implementation are available from the corresponding author upon reasonable request.

References

[1] Bendsøe, M.P.: Optimal shape design as a material distribution problem. Structural Optimization **1**(4), 193–202 (1989) https://doi.org/10.1007/BF01650949

[2] Bendsøe, M.P., Sigmund, O.: Topology Optimization: Theory, Methods, and Applications. Springer, Berlin (2003). https://doi.org/10.1007/978-3-662-05086-6

[3] Sigmund, O., Maute, K.: Topology optimization approaches: A comparative review. Structural and Multidisciplinary Optimization **48**, 1031–1055 (2013) https://doi.org/10.1007/s00158-013-0978-6

[4] Sims, K.: Evolving virtual creatures. In: Proceedings of the 21st Annual Conference on Computer Graphics and Interactive Techniques (SIGGRAPH '94), pp. 15–22 (1994). https://doi.org/10.1145/192161.192167

[5] Cheney, N., MacCurdy, R., Clune, J., Lipson, H.: Unshackling evolution: evolving soft robots with multiple materials and a powerful generative encoding. In: Proceedings of the 15th Annual Conference on Genetic and Evolutionary Computation (GECCO '13), pp. 167–174 (2013). https://doi.org/10.1145/2463372.2463404

[6] Bhatia, J., Jackson, H., Tian, Y., Xu, J., Matusik, W.: Evolution Gym: A large-scale benchmark for evolving soft robots. In: Advances in Neural Information Processing Systems, vol. 34, pp. 2201–2214 (2021). https://proceedings.neurips.cc/paper/2021/hash/118921efba23fc329e6560b27861f0c2-Abstract.html

[7] Hu, Y., Liu, J., Spielberg, A., Tenenbaum, J.B., Freeman, W.T., Wu, J., Rus, D., Matusik, W.: ChainQueen: A real-time differentiable physical simulator for soft robotics. In: 2019 International Conference on Robotics and Automation (ICRA), pp. 6265–6271 (2019). https://doi.org/10.1109/ICRA.2019.8794333

[8] Spielberg, A., Zhao, A., Du, T., Hu, Y., Rus, D., Matusik, W.: Learning-in-the-loop optimization: End-to-end control and co-design of soft robots through learned deep latent representations. In: Advances in Neural Information Processing Systems, vol. 32, pp. 8284–8294 (2019). https://proceedings.neurips.cc/paper/2019/hash/438124b4c06f3a5caffab2c07863b617-Abstract.html

[9] Sato, Y., Kobayashi, H., Yuhn, C., Kawamoto, A., Nomura, T., Kikuchi, N.: Topology optimization of locomoting soft bodies using material point method. Structural and Multidisciplinary Optimization **66**, 50 (2023) https://doi.org/10.1007/s00158-023-03502-2

[10] Yuhn, C., Sato, Y., Kobayashi, H., Kawamoto, A., Nomura, T.: 4D topology optimization: Integrated optimization of the structure and self-actuation of soft bodies for dynamic motions. Computer Methods in Applied Mechanics and Engineering **414**, 116187 (2023) https://doi.org/10.1016/j.cma.2023.116187

[11] Acary, V., Brogliato, B.: Numerical Methods for Nonsmooth Dynamical Systems: Applications in Mechanics and Electronics. Lecture Notes in Applied and Computational Mechanics, vol. 35. Springer, Berlin, Heidelberg (2008). https:

//doi.org/10.1007/978-3-540-75392-6

[12] Kaufman, D.M., Sueda, S., James, D.L., Pai, D.K.: Staggered projections for frictional contact in multibody systems. ACM Transactions on Graphics **27**(5), 164 (2008) https://doi.org/10.1145/1409060.1409117

[13] Kanno, Y., Martins, J.A.C., Costa, A.: Three-dimensional quasi-static frictional contact by using second-order cone linear complementarity problem. International Journal for Numerical Methods in Engineering **65**(1), 62–83 (2006) https://doi.org/10.1002/nme.1493

[14] Kanno, Y.: Primal-dual algorithm for quasi-static contact problem with Coulomb's friction. Journal of the Operations Research Society of Japan **65**(1), 1–22 (2022) https://doi.org/10.15807/jorsj.65.1

[15] Saxcé, G., Feng, Z.-Q.: The bipotential method: A constructive approach to design the complete contact law with friction and improved numerical algorithms. Mathematical and Computer Modelling **28**(4–8), 225–245 (1998) https://doi.org/10.1016/S0895-7177(98)00119-8

[16] Martins, J.R.R.A., Hwang, J.T.: Review and unification of methods for computing derivatives of multidisciplinary computational models. AIAA Journal **51**(11), 2582–2599 (2013) https://doi.org/10.2514/1.J052184

[17] Amos, B., Kolter, J.Z.: OptNet: Differentiable optimization as a layer in neural networks. In: Proceedings of the 34th International Conference on Machine Learning (ICML). PMLR, vol. 70, pp. 136–145 (2017). https://proceedings.mlr.press/v70/amos17a.html

[18] Avila Belbute-Peres, F., Smith, K.A., Allen, K.R., Tenenbaum, J.B., Kolter, J.Z.: End-to-end differentiable physics for learning and control. In: Advances in Neural Information Processing Systems, vol. 31, pp. 7178–7189 (2018). https://proceedings.neurips.cc/paper/2018/hash/842424a1d0595b76ec4fa03c46e8d755-Abstract.html

[19] Geilinger, M., Hahn, D., Zehnder, J., Bächer, M., Thomaszewski, B., Coros, S.: ADD: Analytically differentiable dynamics for multi-body systems with frictional contact. ACM Transactions on Graphics **39**(6), 190 (2020) https://doi.org/10.1145/3414685.3417766

[20] Wächter, A., Biegler, L.T.: On the implementation of an interior-point filter line-search algorithm for large-scale nonlinear programming. Mathematical Programming **106**, 25–57 (2006) https://doi.org/10.1007/s10107-004-0559-y

[21] Hintermüller, M., Ito, K., Kunisch, K.: The primal-dual active set strategy as a semismooth Newton method. SIAM Journal on Optimization **13**(3), 865–888 (2003) https://doi.org/10.1137/S1052623401383558

[22] Hüeber, S., Stadler, G., Wohlmuth, B.I.: A primal-dual active set algorithm for three-dimensional contact problems with Coulomb friction. SIAM Journal on Scientific Computing **30**(2), 572–596 (2008) https://doi.org/10.1137/060671061

[23] Griewank, A., Walther, A.: Evaluating Derivatives: Principles and Techniques of Algorithmic Differentiation, 2nd edn. SIAM, Philadelphia (2008). https://doi.org/10.1137/1.9780898717761

[24] Sagebaum, M., Albring, T., Gauger, N.R.: High-performance derivative computations using CoDiPack. ACM Transactions on Mathematical Software **45**(4), 38 (2019) https://doi.org/10.1145/3356900

[25] Gast, T.F., Schroeder, C., Stomakhin, A., Jiang, C., Teran, J.M.: Optimization integrator for large time steps. IEEE Transactions on Visualization and Computer Graphics **21**(10), 1103–1115 (2015) https://doi.org/10.1109/TVCG.2015.2459687

[26] Li, M., Ferguson, Z., Schneider, T., Langlois, T., Zorin, D., Panozzo, D., Jiang, C., Kaufman, D.M.: Incremental potential contact: Intersection- and inversion-free, large-deformation dynamics. ACM Transactions on Graphics **39**(4), 49 (2020) https://doi.org/10.1145/3386569.3392425

[27] Hüeber, S., Wohlmuth, B.I.: A primal-dual active set strategy for non-linear multibody contact problems. Computer Methods in Applied Mechanics and Engineering **194**(27–29), 3147–3166 (2005) https://doi.org/10.1016/j.cma.2004.08.006

[28] Qi, L., Sun, J.: A nonsmooth version of Newton's method. Mathematical Programming **58**(1–3), 353–367 (1993) https://doi.org/10.1007/BF01581275

[29] Chambolle, A., Pock, T.: A first-order primal-dual algorithm for convex problems with applications to imaging. Journal of Mathematical Imaging and Vision **40**, 120–145 (2011) https://doi.org/10.1007/s10851-010-0251-1

[30] Kanno, Y.: An accelerated Uzawa method for application to frictionless contact problem. Optimization Letters **14**(7), 1845–1854 (2020) https://doi.org/10.1007/s11590-019-01481-2

[31] Bruyneel, M., Duysinx, P.: Note on topology optimization of continuum structures including self-weight. Structural and Multidisciplinary Optimization **29**, 245–256 (2005) https://doi.org/10.1007/s00158-004-0484-y

[32] Le, C., Norato, J., Bruns, T., Ha, C., Tortorelli, D.: Stress-based topology optimization for continua. Structural and Multidisciplinary Optimization **41**, 605–620 (2010) https://doi.org/10.1007/s00158-009-0440-y

[33] Christianson, B.: Reverse accumulation and attractive fixed points. Optimization Methods and Software **3**(4), 311–326 (1994) https://doi.org/10.1080/10556789408805572

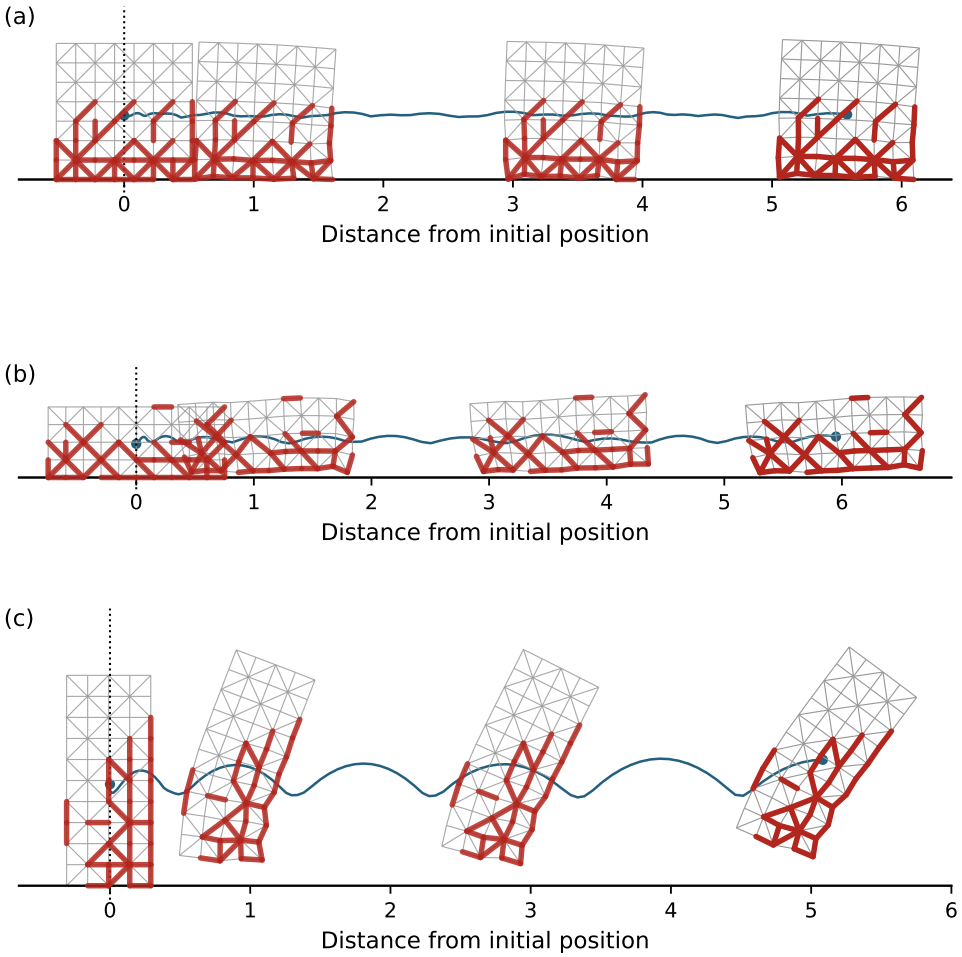


Fig. 6: Motion over the evaluation interval. (a) Square, (b) wide, and (c) tall. Configurations at time steps 0, 33, 67, and 100 are shown in a ground-fixed coordinate system. The blue curve shows the trajectory of the mass-weighted center of mass, the dotted line indicates the initial position of the center of mass, and the horizontal axis represents displacement from the initial position.

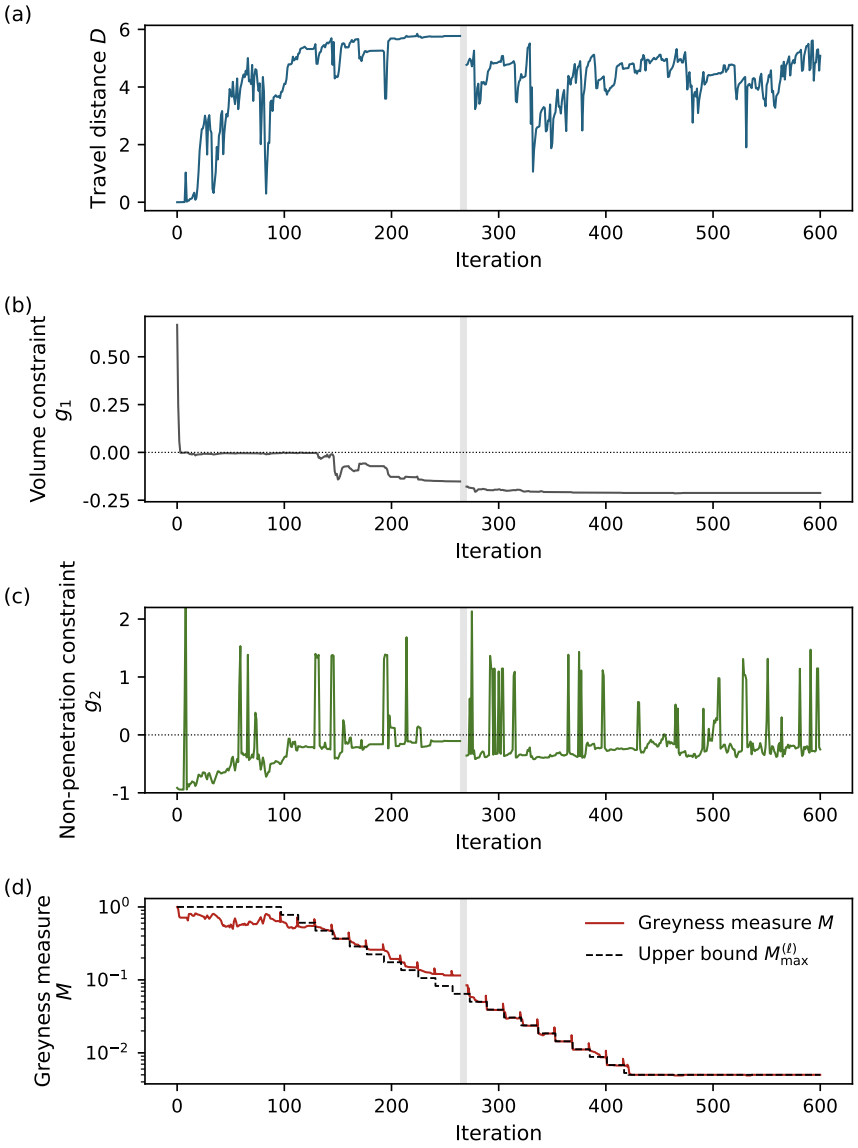


Fig. 7: Iteration history for the tall configuration. (a) Travel distance D. (b) Volume constraint g_1 (satisfied when at most 0). (c) Nonpenetration constraint g_2 (satisfied when at most 0). (d) Greyness measure M and its upper bound $M_{\max}^{(\ell)}$, which is reduced in stages (logarithmic scale). Grey bands indicate intervals in which iterations are not recorded because the interior-point method is in its feasibility-restoration phase.

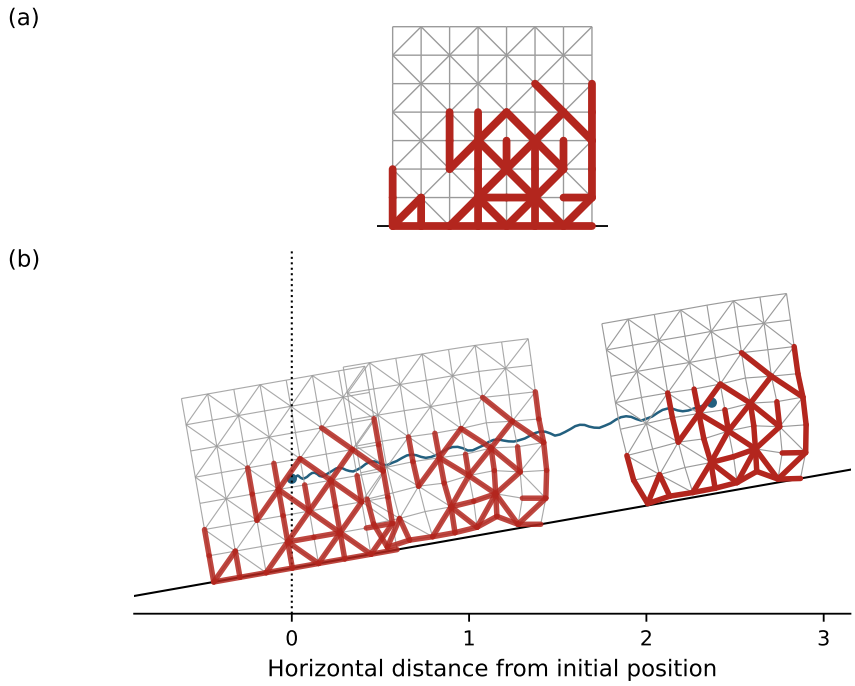


Fig. 8: Optimized square design and its motion on an uphill slope with an inclination of 10°. (a) Final design, with structural members shown in grey and actuator members shown in red. (b) Motion over the evaluation interval. Configurations at time steps 0, 50, and 100 are shown. The blue curve represents the trajectory of the mass-weighted center of mass, the dotted line denotes the initial position of the center of mass, and the horizontal axis denotes the horizontal displacement from the initial position.

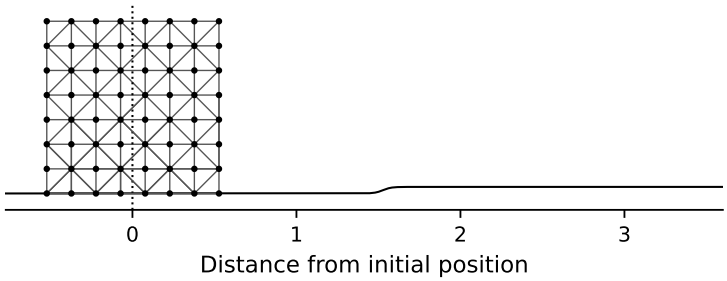


Fig. 9: Ground profile with a step. The walker is shown in its initial configuration. The dotted line denotes the initial position of the mass-weighted center of mass, and the horizontal axis represents the horizontal displacement from the initial position.

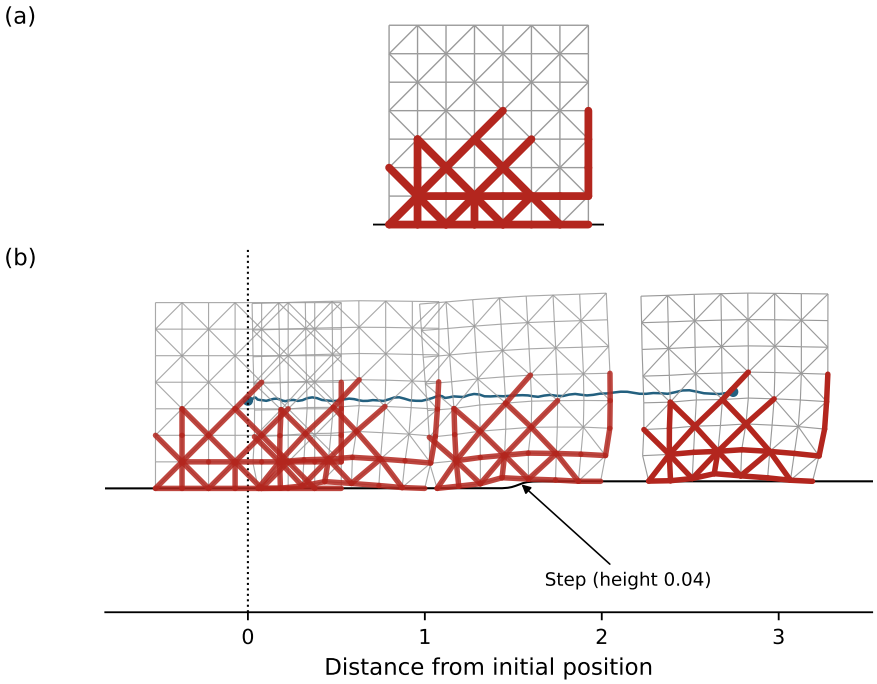


Fig. 10: Optimized square design and its motion over ground with a step. (a) Final design, with structural members shown in grey and actuator members shown in red. (b) Motion over the evaluation interval. Configurations at time steps 0, 33, 67, and 100 are shown in a ground-fixed coordinate system. The arrow indicates the step location, the blue curve represents the trajectory of the mass-weighted center of mass, the dotted line denotes the initial position of the center of mass, and the horizontal axis represents horizontal displacement from the initial position.